Data quality of collocated portable broadband seismometers using direct burial and vault emplacement

Kasey Aderhold[1], Katherine E. Anderson[2], Angela M. Reusch[2], Mary C. Pfeifer[2], Richard C. Aster[3], and Tim Parker[2]

Corresponding author: Kasey Aderhold, Department of Earth and Environment, Boston University, 685 Commonwealth Avenue, Room 130, Boston, MA 02215, USA. (kasey@bu.edu)

[1]Department of Earth and Environment, Boston University, Boston, Massachusetts, USA.

[2]Incorporated Research Institutions for Seismology Program for Array Seismic Studies of the Continental Lithosphere Instrument Center, Socorro, New Mexico, USA.

[3]Geosciences Department, Colorado State University, Fort Collins, Colorado, USA.

Kasey Aderhold, Katherine E. Anderson, Angela M. Reusch, Mary C. Pfeifer, Richard C. Aster, Tim Parker; Data Quality of Collocated Portable Broadband Seismometers Using Direct Burial and Vault Emplacement. *Bulletin of the Seismological Society of America*; 105 (5): 2420–2432. doi: https://doi.org/10.1785/0120140352

Data quality of co-located portable broadband seismometers using direct burial and vault emplacement

Kasey Aderhold[1], Katherine E. Anderson[2], Angela M. Reusch[2], Mary C. Pfeifer[2], Richard C. Aster[3], and Tim Parker[2]

Corresponding author: Kasey Aderhold, Department of Earth and Environment, Boston University, 685 Commonwealth Avenue, Room 130, Boston, MA 02215, USA. (kasey@bu.edu)

[1]Department of Earth and Environment, Boston University, Boston, Massachusetts, USA.

[2]Incorporated Research Institutions for Seismology Program for Array Seismic Studies of the Continental Lithosphere Instrument Center, Socorro, New Mexico, USA.

[3]Geosciences Department, Colorado State University, Fort Collins, Colorado, USA.

Electronic Supplement:

The supplementary material for this paper contains figures of the daily median noise levels in the microseism band, monthly probability density functions for the magnitude squared coherence between the six station couplings [Direct Burial 1 to Direct Burial 2, Vault 1 to Direct Burial 1, Vault 1 to Direct Burial 2, Vault 1 to Vault 2, Vault 2 to Direct Burial 1, Vault 2 to Direct Burial 2] for all three components [BHE, BHN, BHZ], results of the coherency self-noise analysis, and the recordings of the teleseismic and local earthquakes used for the signal-to-noise analysis.

Abstract

Temporary broadband sensor deployments have traditionally been predominantly emplaced using shallow vaults that require more materials, personnel, and time than direct burial. However, new developments in seismometer and seismograph technology are increasingly facilitating systems that can be directly buried in earth or snow without vault enclosures. We analyze data from two identical shallow vaults installed adjacent to two identical direct burial sites in soft flood plain alluvial and shallow water table conditions near Socorro, New Mexico. Data recorded from these four sensors over eight months in 2012 were assessed to determine if the emplacement type had a significant and systematic effect on data quality. We used metrics derived from power spectral density analysis to examine temporal trends in noise [instrument, installation, and site noise], signal-to-noise ratio for teleseismic and local earthquakes, and magnitude squared coherence of both noise and earthquake signal recordings. We found that noise on the vault sensors is higher during the transition from spring to summer than for the direct burial sensors. This difference is especially evident on the horizontal components at long periods between 20-170 seconds with an average of 5.3 dB more noise on the vaults than the direct burials from April to June, indicating enhanced tilt susceptibility for vault emplaced sensors. However, most variability in data quality is comparable between sensors with differing emplacement methods and between sensors with the same emplacement method in this four-station experiment. We conclude that the direct burial emplaced sensors at this test site performed as well as the vault emplaced sensors, and that direct burial is preferable when considering data quality and ease of installation.

Introduction

Temporary broadband seismic deployments have been driving advancements in seismological investigation into seismic sources and earth structure for decades (e.g., Aster et al., 2005). The emplacement method of choice for temporary broadband deployments has overwhelmingly been a shallow vault-style design, where a hole that is substantially larger than the seismometer is excavated to accommodate bulky installation materials. The vault is designed to protect the sensor from the elements, insulate it from temperature and surface noise, and to couple the sensor stably with the ground (Trnkoczy et al., 2002). Vault-style sensor emplacement often requires significant manpower, installation times of hours to days, and materials that cost hundreds of dollars or more per site. Direct burial emplacement, in contrast, requires an augered or otherwise excavated hole that is only slightly larger than the instrument itself and approximately one hour or less to install a station, while utilizing a fraction of the manpower, tools, and materials. To assess if direct burial is a feasible cost- and time-attractive emplacement alternative to vaults while not compromising data quality, we present a quantitative comparison between data recorded by co-located sensors using the two emplacement types. Four identical broadband sensors were installed in two identical shallow vaults and two identical direct burial sites in close proximity at an alluvial high soil moisture location near Socorro, New Mexico. Eight months of data recorded during 2012 from these four sensors were intercompared to determine any systematic quality differences using metrics derived from power spectral density analysis, signal-to-noise ratios, and magnitude squared coherence. These data quality metrics were also monitored with time, given that sudden but inevitable seasonal changes such as freeze-thaw, soil moisture levels, and high winds are likely to have different effects on sensors installed in different emplacement conditions.

Site Selection

The installation location [33.96ºN, 106.85ºW] is a “soft” site characterized by ~1.2 meters of recent mud and silt floodplain deposits overlying deeper alluvial fill of the central Rio Grande rift (Cather, 2002). This area is prone to flooding from the river and from adjacent arroyos, and the water table is shallow, varying from many centimeters to several meters deep, depending on the season. Sources of local seismographic noise are likely to include wind, variations in precipitation and soil moisture, temperature cycles, nearby riparian (cottonwood and tamarisk) vegetation, a natural gas pipeline within 2 km, as well as seismic and tilt coupling from vegetation and grazing cattle that may sporadically come within meters of the site (Anderson et al., 2012). Two Program for Array Seismic Studies of the Continental Lithosphere (PASSCAL)-style shallow vaults and two direct burial deployments were co-located within a 4 m-square area, Figure 1a-b. All deployments used Güralp CMG-3T sensors with a long-period corner frequency of 120 s and a gain of 1500 V/m/s. CMG-3Ts are not designed for direct burial, but the two directly buried sensors in this experiment were retrofitted with waterproof cable connectors and cables. Data were collected on two 6-channel Quanterra Q330 digitizers with 1 Hz and 40 Hz sampling and telemetered to the nearby PASSCAL Instrument Center at New Mexico Tech in Socorro. Data were subsequently archived at the Incorporated Research Institutions for Seismology (IRIS) Data Management Center under the YE temporary network code. The site was powered with four 65-W solar panels and two 100-A-Hr lead acid batteries contained, along with the dataloggers, charge controllers and cell modem, in a very small aperture terminal (VSAT) box sited next to the sensors. A posthole sensor was also installed within the site during the study, but recordings from this station are not analyzed here.

The PASSCAL-style shallow vaults (Figure 1a) consisted of concentric plastic barrels: an inner 15-gallon with an open bottom for housing the sensor and an outer 55-gallon with a locking lid. Both barrels were installed in the ground over a 20 cm high cement pier with open-cell foam and styrofoam disks for thermal insulation and air circulation buffering. The direct burial emplaced sensors were contained in a heavy plastic bag and installed on top of 5 cm of compacted all-purpose sand with fine sand gently tamped around the sensor. The plastic bag covering the direct burial sensors was later removed after it was deemed not necessary for protection. Additional dirt was mounded on top of the sensor installations to provide further insulation and thermal mass to minimize temperature fluctuations. The installation was then covered with a tarp for protection from rain. The vault and the direct burial sensors were both situated at a depth of about 1 m from the top of the mounded dirt to the sensor base. Sensor specifications are reported in Table 1.

Data Return

There were two sensor failures that occurred during this study, with Direct Burial 2 (Table 1) performing poorly beginning on 22 September 2012, and continuing through November, as well as a failure with the BHE component of Direct Burial 1 on 18 November 2012. A conclusive reason for the failure of the direct burial sensors during this study could not be determined, though both instruments failed most significantly on the BHE component. Lightning strikes were investigated as a possible cause, however there were no storm cells or lightning strikes reported within three days of either failure (U.S. National Lightning Detection Network™ and NEXRAD, accessed 8 April 2014). A compromised power source may be the cause of a failure. Data recorded during the eight-month period from 1 January 2012 to 31 August 2012, excluding a telemetry gap on 17 January 2012, was chosen for the analysis to utilize periods of time when all sensors were functioning properly.

Data Quality Analysis

Eight months of data from January to August 2012 recorded on all four emplaced sensors were compared to determine if the two emplacement methods showed a systematic effect on data quality. To do this we calculated power spectral density, signal-to-noise ratio for teleseismic and local earthquakes, coherence of the sensors for both noise and earthquake signal recordings, and also monitored and accounted for any discrepancies in data return. This analysis was focused on assessing use of such data in research, as well as examining relevant temporal trends in data quality at scales from seconds to seasons.

Power Spectral Density

To characterize seismic noise levels, we used the method of McNamara et al. (2009) to compare baseline data qualities through power spectral density (PSD) probability density function (PDF) analysis. PSDs were calculated using PQLX software (McNamara and Boaz, 2011) using continuous one-hour time series segments of data overlapping by 50%, resulting in 48 PSDs per day per sensor. The instrument response was deconvolved from the signal to allow comparison of the calculated PSDs to the New Low Noise Model (NLNM) and New High Noise Model (NHNM) (Peterson, 1993), baselines for seismic station performance that remain widely used despite more recent proposed models (McNamara and Buland, 2004; Berger et al., 2004; Castellaro and Mulargia, 2012). Earthquake and most other signals are highly sporadic, so robust central tendency estimates for the background noise at a seismic station are best characterized using the median of the PDFs at each frequency interval without resorting to event culling.

Median PSD PDFs from eight months of data for each sensor are reported in Figure 2a. There was not a perceptible difference between the overall trends of the 10th and 90th percentiles of the PDFs and the medians of the PDFs. The site may be generally characterized, relative to the Peterson noise models, as being high noise at shorter periods. The high horizontal/vertical noise ratio observed here is typical of shallow vaults (e.g., Anthony et al., 2015), and reflects the coupling of local tilt into horizontal component signals (e.g., Wielandt and Frobriger, 1999). As is often observed, long-period vertical site noise is more coherent than the long-period horizontal site noise. The median PSD PDFs of all eight months of data show that the direct burial sites had highly comparable noise levels to the vaults except for the horizontal components at long periods [15 s ≤ T] where the east component of both of the direct burials had less noise than the vaults.

To highlight differences between the recorded noise levels more clearly, the mean was taken of the four median PSDs of the direct burial and vault sensors for each respective component at each frequency to calculate an average comparison PSD of all stations. The difference between this all-station average PSD and the median PSD of each sensor was then calculated at each frequency, with negative values showing a higher probability of less noise power than the average and positive values showing a higher probability of more noise power than the average (Figure 2b). This analysis shows that the predominant difference in noise level is on the east component where the median power levels of both direct burial stations at periods greater than 15 s are at least 2 dB lower than both vault stations. Between the highest noise vault station and the lowest noise direct burial station on the east component this performance difference grows to about 9 dB at 100 s. The north component does not show this effect, with

Direct Burial 1 performing similarly to the vault stations and only Direct Burial 2 having lower noise. There is some separation in station performance at longer periods on the vertical component, but all station medians stay within a 4 dB spread of each other at all periods. At periods less than 10 s on all three components, all four stations stay within 1 dB of the ensemble mean.

Temporal trends in background noise are also an important metric of consistent station performance. Daily temperature cycles and weather patterns change strongly with the season in central New Mexico, with winter months potentially bringing the effects of ground freeze and thaw, spring months characterized by high winds, and summer months heralded by monsoon rains. To explore how these seasonal changes affect the data quality of the differing emplacement types at this site, median PSD PDFs were taken for each day and divided into three useful period bands: short period [0.1-1 s], microseism [2-20 s], and long period [20-172 s]. Dividing the result into separate frequency bands is valuable, as there is a strong frequency-dependence on sources of noise and the performance of these stations. These differing bandwidths are also distinctly important to a variety of research applications. Median daily PSD PDFs were interpolated, and the difference between the PSD and the NLNM was calculated at each frequency from 0.1 to 172 s. This difference between daily PSD PDFs and the NLNM was then averaged across each band to create basic seasonal noise level metrics. Since all sensors are compared to the same baseline noise model, these differences can then be compared to one another and provide an accurate average power, or power difference, of the noise for each day. This analysis was performed on all three components of the four sensors in the study and the results of the microseism and long period band are reported in Figure S1 of the electronic supplement to this article and Figure 3 respectively.

It is well known that teleseismic body waves have a contribution to ambient seismic background through extended coda and aftershock signals that confer small amplitude motion to the surface over a long period of time, and it is possible that this phenomenon is measurable in this analysis (Boué et al., 2013). Days on which a $M_W \geq 7$ earthquake occurred are indicated and while every $M_W \geq 7$ earthquake does not mark a day of higher than average noise, many high noise days do line up with an $M_W \geq 7$ earthquake and we disregard these days to concentrate on locally- or regionally-generated background power trends.

The vertical component is ubiquitously the lowest noise component usually with a separation from the horizontals of at least 20 dB, while the noisier east and north components overlap one another (Figure 3). Some of the distinct trends on the vertical component of Direct Burial 2 may be due to the drift of the sensor's mass position, which can add long-period noise on the vertical component of CMG-3T sensors. This prompts a mass re-center command from the data logger and a corresponding abrupt decrease in vertical noise after the sensor settles. If a gradual increase in vertical long-period noise follows the trend of vertical mass-position drift and an abrupt decrease in vertical long-period noise coincides with a mass re-center and mass voltage decrease, then the long-period vertical noise is almost certainly related to mass position. Mass re-centers were triggered by the horizontals of Direct Burial 2 on 8 March and 10 June 2012, coinciding with a drop in the vertical long-period noise of the station. An additional mass re-center on 1 August 2012 does not show a clear drop in long-period noise.

The horizontal components of all four sensors show a decrease in noise in the microseism band from April through August in Figure S1 available in the electronic supplement to this paper, reflective of a typical seasonal decrease in Northern Pacific storms during that time period (e.g., Aster et al., 2008; Given, 1990; Hasselmann, 1963). The horizontal components of the direct burials showed an average decrease of 3.6 dB from January-March to April-June on the horizontal components compared with an average decrease of only 1.9 dB on the vault sensors. On the long period band the two direct burial sensors display fairly consistent noise levels with a decrease of noise from April to June on the horizontal components consistent with this scenario. The vaults, however, show a general increase in noise beginning in April in the long period band, which tapers off through August. On average the horizontal components of the vaults have 5.3 dB more noise from April to June than the direct burials at long periods. The source of this noise is likely local environmental effects occurring in the spring months. Average maximum-minimum temperature differentials are highest during April, May, and June with a 36ºF monthly average differential during this time period, 4ºF greater than the average temperature differential of all other months (Arguez et al., 2012). The experimental site is also very near the Rio Grande, with clay-rich alluvium and a variable and shallow water table. Discharge is mainly driven by snowmelt and is recorded on two United States Geological Survey (USGS) water data sites near the sensors, one 18.2 km directly north and one 3.7 km directly south. These sites show identical trends, with a relatively steady daily discharge of 700 ft^3/s from January through March, disrupted on 4 April 2012 by the largest spike to over 2000 ft^3/s followed by lesser spikes of 1500, 1000, and 700 ft^3/s before decreasing to zero flow by the end of July (USGS New Mexico Water Science Center National Water Information System, last accessed 19 February 2015). During demobilization we observed evidence of repeated flooding from the interior floor of the vaults, with water levels to within 15 cm of the top of the cement pier. Residue of previous moisture beads on the interior top of the inner barrel of the vaults and moisture on the inside of the open-cell foam was also found, but there was no evidence of water flowing in from the top of the vault so we concluded that water must have entered through the base. The direct burial sensors were above this inferred maximum water table. Repeated wetting and drying of the clay-heavy sediment from changes in the average discharge of the Rio Grande could be responsible for the increase in observed long-period noise observed on the vault sensors in the spring months.

Magnitude Squared Coherence

A useful metric for intercomparing the similarity of signals at co-located seismic stations is to calculate their coherency, a fundamental measure of how similar the phase and amplitude structure of time series data are as a function of frequency. Values of coherency between two time series range from near 0, indicating incoherence and 1 indicating perfect resemblance. The complex coherency function is the cross-spectral power density function normalized by the square root of the product of the power spectral density functions of the two time series to be compared. The cross spectrum is the discrete Fourier transform of the cross correlation function between two time series X and Y, where the cross correlation is:

$$R_{xy}(n) = \sum_{t=-\infty}^{\infty} X(t)Y(t-n)$$

and the cross spectrum is the Fourier transform of the cross correlation at a specific angular frequency ω:

$$P_{xy}(\omega) = \sum_{k=-\infty}^{\infty} R_{xy}(m)e^{-j\omega k}$$

The angular frequency ω can be converted to frequency f by the simple relation:

$$\omega = 2 * \pi * f$$

Magnitude squared coherence $C_{xy}\left(f\right)$ (MSC) is calculated in this study given by:

$$C_{xy}(f) = \frac{\left|P_{xy}(f)\right|^2}{P_{xx}(f)P_{yy}(f)}$$

where $P_{xy}(f)$ is the cross spectrum of the two equally sampled time series X and Y, and their associated power spectral densities are noted by $P_{xx}(f)$ and $P_{yy}(f)$ respectively. MSC was calculated for each hour of data recorded from January through August of 2012, using the Welch's overlapped averaged periodogram method (Welch, 1967) with 1-hour windows, an overlap of 30 minutes, and a standard Hamming window. With three components [BHE, BHN, BHZ] and three station couplings [Vault 1 to Vault 2, Direct Burial 1 to Direct Burial 2, and Vault 1 to Direct Burial 1] there were 9 interstation same-component comparisons.

Probability density functions of MSC were produced from the ensemble of hourly MSC estimates for each station/channel comparison, for each month. The median of this PDF was then evaluated as a representative MSC metric as a function of frequency (Figure 4). Figures for all six station couplings of the monthly probability density functions for MSC are available in the electronic supplement to this article and allow the temporal changes to be observed.

Effect of Orientation Error on MSC

Seismic sensors are typically installed with great precision and care, however orientation errors occur in the field and can be up to 10º (Ekström and Busby, 2008). Sensor alignment errors can add a significant amount of uncorrelated noise on the horizontal components, and slight variations from the vertical allow noise to leak onto the vertical component particularly in the microseism band (Ringler et al., 2011). In order to determine the relative orientation of the four sensors in this study, we use a modified version of the coherency analysis method by Sleeman et al. (2006). Vault 1 was used as the reference station and hourly data segments from 1 - 31 December 2011 were used to minimize both noise and temperature fluctuations (Ringler et al., 2011). Data from the other vaults were rotated in the horizontal plane by increments of 0.1º until the uncorrelated instrument and site noise in the microseism band [3 s to 30 s] median power across all hourly segments was minimized for each individual sensor relative to the data collected at Vault 1. The optimal rotations for each sensor in the clockwise direction relative to Vault 1 were -4.4º, 3.1º, and -2.4º for Vault 2, Direct Burial 1, and Direct Burial 2 respectively. These orientation errors are similar to those found for many Advanced National Seismic System stations prior to 2011, and are attributed to uncertainties arising from the use of a magnetic compass to estimate horizontal orientation during sensor deployment (Ringler et al., 2013). The remaining uncorrelated noise levels of the direct burial sensors were within a few decibels of the vaults sensors, with an improvement over the vault sensors in the long periods of 10 seconds or greater on the BHE component.

A significant amount of uncorrelated noise remained in the microseism band on the BHZ component after the rotation in the horizontal plane, prompting a further rotation of the data to minimize uncorrelated noise in the vertical plane using the same methodology as for the horizontal components. The vertical rotation was done iteratively for dip and azimuth with increments of 0.05º and 1º respectively. The rotations that minimized the uncorrelated microseism noise were dips and azimuths of 0.2º/10º, 0.35º/175º, 0.4º/20º, and 0.3º/125º for the Vault 1, Vault 2, Direct Burial 1, and Direct Burial 2 respectively. Any tilt noise from off-vertical alignment on this scale is negligible for the previous temporal noise analysis due to these small angles. The uncorrelated noise that remained in the microseism was higher in the direct burials and the noise that remained in the long periods was higher in the vaults. This incoherent noise can come from additional sources other than the seismic wavefield alone, such as non-seismic vault-localized ground strains in a relatively high noise site (Ringler et al., 2011). Other results from this analysis are available in the electronic supplement to this article.

To ensure that our results are not affected by calculating the MSC of misaligned stations, we tested the effect of orientation errors on MSC in a controlled way. We took the recorded data of the BHE component of Vault 1 for the month of December 2011 and rotated it in the horizontal plane by 1º, 2º, 3º, 4º, 5º, 10º, and 20º to simulate a misalignment. We took each rotated recording and performed the same MSC analysis outlined previously on the original Vault 1 data (Figure 5a-b). Calculating the coherence of the original signal to the slightly rotated signal is a method that fully isolates the effects from a misaligned sensor. Misalignment of the vertical plane was also tested for eastward dips of 0.2º, 0.4º, 0.8º, 1.6º, and 3.2º from the vertical (Figure 5c-d). The effects in MSC for rotations of the horizontal plane from 1º-5º were minimal with a maximum 0.01 decrease in MSC at frequencies of 0.3 and 2 Hz. Similarly, MSC was only reduced by a maximum of ~ 0.015 with a 0.4º rotation of the vertical plane and only at the longest frequencies. With larger rotations in both the horizontal and vertical plane, reductions of MSC are more significant. The maximum orientation errors of the sensors are less than 5º in the horizontal and 0.4º in the vertical, which equates to an indiscernible effect on MSC based on our calculation above. We conclude that any uncorrected misalignment between sensors will not impact the results of our calculations, but it should be a consideration for stations with larger orientation errors.

Same-emplacement MSC

For all months the vertical components of the direct burial sensors are more consistently coherent with one another than any other component/station pair at longer periods to about 10 s, past which MSC drops off rapidly, Figure 4. This is in contrast to the vertical component of the vaults, which are less consistently coherent but show higher levels of vertical component coherence at longer periods to approximately 100 s. The direct burial vertical components also show consistently higher MSC through the microseism band than the vaults. Both horizontal components show comparable MSC between vault-vault and direct burial-direct burial comparisons during all months at periods above 10 s, excluding a dip at 1 Hz. The 1 Hz frequency is often associated with cultural noise, but this decrease in coherency may also be due to wind noise (Wilson et al., 2002; Given, 1990). Temporal trends of MSC can be best observed in the animated plots available in the electronic supplement to this article in Figures S2-S4. From June to August, the coherence of direct burial-to-direct burial horizontal components stay steady at 1 Hz while the vault-to-vault decrease in coherence. This difference could be due to the additional 30+ cm of thermal mass above the direct buried sensors, providing more protection from temperature changes in the summer months. At periods longer than 10 s, the coherence of direct burial-to-direct burial horizontal components vary up to 0.3 in MSC while the vaults vary up to 0.6 in MSC between January and June.

Dissimilar-emplacement MSC

When dissimilar emplacement type sensors are compared, we find that MSC is comparable to the analysis done in the previous section with similar emplacement types at periods higher than 10 s for all three components, Figure 4. The one exception is a drop around 1 s in MSC between Vault 1 and Direct Burial 1 on the BHE component during August. On the vertical component at periods longer than 50 s, the MSC is higher between Vault 1 and Direct Burial 1 than MSC between Direct Burial 1 and Direct Burial 2. Thus, MSC in recorded signals can be lower between two sensors with the same emplacement than two sensors with different emplacement in this experiment.

Hourly MSC

Hourly MSC values were integrated across three frequency bands of 0 to 0.2 Hz, 0.2 to 5 Hz and 5 to 20 Hz to produce coherency metrics for the long period, microseism and short period bands, Figure 6a. These integrated values were normalized by the ideal magnitude squared coherence to compare the three bands to one another (Anderson et al., 2012). Coherence values of zero indicate the data gaps on 17 January 2012. The short period and long period bands are much less coherent than the microseism band, rarely dipping below 0.8 coherence in both vault-to-vault and direct burial-to-direct burial over all months and all three components. Short period coherence typically falls around 0.7 for all stations and all components. The BHE components show the most temporal change in behavior in the long period band with a range in coherency of 1.0-0.6 coherence in January at both station pairings increasing to a range of 1.0-0.5 for direct burial-direct burial and 1.0-0.3 for vault-vault coherence in June. These temporal changes in coherence are well-above the uncorrelated noise of the sensors from misalignment, suggesting that these sensors are recording a source of noise that changes in coherence temporally and is recorded differently based on emplacement type.

To investigate temporal cycling of coherence, each month of hourly coherences was converted to the frequency domain by taking the fast Fourier transform for each band and for all six vault and direct burial station pairings (Figure 6b). A distinct diurnal cycle can be identified at the 0-0.2 Hz band, evident in the sinusoidal pattern of the lowest frequency plots on both the direct burial and vault in June, Figure 6a. The strongest cycle appears in the lowest frequency band for all components, with the highest amplitude corresponding to a daily cycle on the east component (Figure 6b). The vertical component (not shown) displays only a slight diurnal peak on the lowest frequency band, less than one third the amplitude of the east component. The amplitude of the daily cycle increases in the later months with the highest amplitude in August. This daily cycle of long period noise could be explained by temperature and atmospheric pressure, both diurnally varying factors known to cause uncorrelated noise on sensors (Custódio et al., 2014; Sleeman and Melichar, 2012; Given, 1990). We believe that the decline in MSC of the direct burial sites in June at long periods is due to wind driven spatially variable strain such as ground tilt from tree roots. Relationships between environmental factors, emplacement type, and noise require further analysis.

Signal-to-Noise (SNR)

The ratio of earthquake signal-to-noise (SNR) recorded by sensors is included in this study because the most common use of PASSCAL seismic stations is to record earthquakes. Teleseismic earthquakes were taken from the National Earthquake Information Center (NEIC) global earthquake search and were selected for $M_W \geq 6$ and within distances of 30º to 90º from the installation site. 23 teleseismic earthquakes representing a wide range of depths and faulting styles were used in this analysis, evident from their global Centroid Moment Tensor mechanisms (Ekström et al., 2012). Local earthquakes were taken from the New Mexico Tech Seismological Observatory earthquake archives with distances up to 10 km from the site, representing magnitudes of $1.1 \geq M_L \geq 0.1$. Six of these local earthquakes had a clear onset to distinguish the event signal from the noise and were included in the analysis. The vertical waveforms were filtered with a second-order, single-pass band-pass filter between 0.5 Hz and 3 Hz for teleseismic events and a second-order, single-pass high-pass filter with a corner of 1 Hz for local events. *P* wave arrivals were calculated to first-order using the TauP Toolkit (Crotwell et al., 1999) with the IASP91 1D earth model (Kennett and Engdahl, 1991) and then were manually repicked. Two windows of data were selected before and after the manually picked arrival for the noise and signal windows, each with lengths of 40 seconds for teleseismic and 1 second for local earthquakes. The signal-to-noise ratio (SNR) was defined as the ratio of the root-mean-square (RMS) of the signal over the RMS of the noise.

All stations have a median SNR of 17 or above and a mean SNR of greater than 26 for teleseismic earthquakes occurring between 1 January and 31 August 2014, recorded on the vertical component (Table 2). Both mean and median are shown, but the median SNR is less biased by the greater signal of the largest earthquakes. The differences of SNR between sensors for these strong teleseisms, not surprisingly, are insignificant for the frequency range of 0.5 – 3 Hz. Both direct burial stations had slightly higher SNR than both vault stations for all six of the local earthquakes but the differences were not significant (Table 3). Recordings of the teleseismic and local earthquakes can be found in Figure S7 and S8 available in the electronic supplement to this paper.

Coherency of pre-event noise and coherency of earthquake signal between the four sensors was compared using the largest event that occurred during the study period, the M_W 7.7 earthquake near Japan on 14 August 2012. The MSC, as defined in the previous section, was taken on the pre-event noise and a signal window defined by 15 minutes of unfiltered data windowed on either side of the *P* arrival, Figure 7. The signal portion is always more coherent than the noise particularly at low frequencies of less than 0.1 Hz but also at high frequencies of about 10 Hz. Signal coherency is of comparable magnitude between all stations pairings, with the dissimilar pairing of Vault 1 and DB 1 showing the highest values. This suggests that emplacement type does not have a detectable impact on the coherence of recorded events between adjacent sensors.

Conclusions

We conclude that in this high-noise and soft-soil site broadband sensors with direct burial emplacement have very similar data quality to co-located sensors with vault emplacement over an eight-month record. Power spectral density (PSD) probability density function (PDF) analysis shows that all components of directly buried sensors have comparable noise levels to sensors emplaced in vaults. However, the sites show differing responses to seasonal changes that we attribute to the soil column, with horizontal components of the direct burial sensors at long periods showing less noise beginning in early April while the vault sensors show increased noise, with these trends continuing into mid-July. This represents an improvement of 5.3 dB in mean noise levels on horizontal components of the direct burial sensors over the vault sensors at long periods during the spring transition, when these moist soils are undergoing vadose zone drying and/or shallow freeze thaw, and indicating that direct burial sensors were in this case more resistant to tilt-coupled noise from these processes.

Diurnal cycling of magnitude squared coherence (MSC) is apparent in both vault and direct burial comparisons, and is most obvious in the long period band of all components starting in mid-July. August shows the widest range of MSC in both emplacement type comparisons, cycling from 0.1 to 1. The MSC probability density functions show that the direct burial-to-direct burial comparisons have a smaller range of coherence values around 1 Hz than the vault-to-vault coherency. This could be explained by atmospheric pressure induced tilt known to produce incoherent signals even at sensors co-located to within 1 meter, as well as increased incoherency due to the vault void space (Ringler et al., 2011).

The signal-to-noise analysis shows similar values for high signal/noise teleseismic events recorded at all four stations as well as for lower signal/noise local events down to M_L of 0.1.

Coherence of the largest recorded earthquake [M_W 7.7] during the field experiment did not appreciably differ between like and dislike emplacement types.

We compare data quality between vault-sited and shallow directly buried sensors to show that the time and cost advantages of direct burial do not appreciably degrade data quality in a soft soil environment. Noise recorded by vault-sited sensors is generally higher in amplitude during the transition from spring to summer as compared to the direct burials. This increase is especially evident on the tilt-coupled horizontal components at long periods between 20-170 s. Levels of noise, and diurnal changes in the levels, are similar at all sensors from cultural activity, wind noise, local tilting, and temperature fluctuations. We conclude that direct burial broadband sensors in this environment were essentially equivalent in data quality to the shallow vaults, and can be superior.

Although this was a closely monitored and maintained site, two directly buried sensors failed on separate occasions. While this does not necessarily indicate that these standard 3T were ill suited for the direct burial environment, we do not endorse directly burying broadband sensors that are not purpose-built for direct burial. This work thus suggests that the community would be well served by developing and deploying robust broadband sensors that can be routinely installed via direct burial using the methods discussed in this paper.

To improve data quality for similar portable broadband sites, we suggest employing a similar augured direct burial technique over vault installation to reduce the cargo load for each installation and to reduce noise from non-seismic sources. Augered posthole design has been utilized for seismic emplacement in icy environments, and includes an “all in one” datalogger and sensor design to further reduce installation materials (Bernsen et al., 2014). Streckeisen STS-4B and Trillium 120PH sensors installed in deeper posthole/borehole systems show improvement over deeper Transportable Array style vaults in the long period band on the horizontal components, and methods for securing the cables and sensors within these configurations have been developed to further improve station performance (Frassetto et al., 2014). These techniques will soon be deployed on a large scale in EarthScope USArray Transportable Array activities in Alaska and Canada (Busby et al., 2013).

Data and Resources

All data used in this study can be obtained under the network code YE from the IRIS Data Management Center at www.iris.edu [last accessed February 2015].

Acknowledgements

The seismic instruments were provided by IRIS through the PASSCAL Instrument Center at New Mexico Tech. The facilities of the IRIS Consortium are supported by the National Science Foundation under Cooperative Agreement EAR-1261681 and the DOE National Nuclear Security Administration. The authors appreciate the valuable comments of two anonymous reviewers that helped to improve this article. Thank you to the numerous researchers and students who contributed to all stages of this long-term project, and especially to the entire staff at IRIS PASSCAL Instrument Center including Noel Barstow, Pnina Miller, George Slad, and Bruce Beaudoin.

References

Anderson, K. E., S. Azevedo, N. Barstow, B. Beaudoin, L. Carothers, J. Gridley, M. Love, P. Miller, T. Parker, C. Pfeifer, A. M. Reusch, G. Slad, and D. Thomas (2013). Preliminary report: PASSCAL sensor emplacement testing at Poker Flats, Alaska, *EarthScope National Meeting*, Raleigh, USA.

Anderson, K. E., J. F. Anderson, R. E. Anthony, J. Chaput, N. D. McMahon, E. A. Morton, C. Pfeifer, M. E. Templeton, J. M. Tarnowski, T. Parker, and R. C. Aster (2012). A site comparison of shallow vault-deployed and direct burial broadband sensors, *Incorporated Research Institutions for Seismology Workshop*, Boise, USA.

Anthony, R., R. Aster, D. Wiens, A. Nyblade, S. Anandakrishnan, A. Huerta, J. P. Winberry, T. Wilson, and C. Rowe (2015). The seismic noise environment of Antarctica, *Seismol. Res. Lett.*, **86** 12 p.

Arguez, A., I. Durre, S. Applequist, R. S. Vose, M. F. Squires, X. Yin, R. R. Heim, and T. W. Owen (2012), NOAA's 1981-2010 U.S. climate normals: An overview. *Bull. Amer. Meteor. Soc.*, **93** 1687-1697.

Aster, R., B. Beaudoin, J. Hole, M. Fouch, J. Fowler, and D. James (2005). IRIS seismology program marks 20 years of discovery, *EOS Trans. AGU,* **86** 171-172.

Aster, R. C., D. E. McNamara, and P. D. Bromirski (2008). Multidecadal climate-induced variability in microseisms, *Seismol. Res. Lett.,* **79**, 194-202.

Berger, J., P. Davis, and G. Ekström (2004). Ambient Earth noise: A survey of the Global Seismographic Network, *J. Geophys. Res*, **109** 1-10.

Bernsen, S., P. Winberry, A. Huerta, R. Aster, R. Woodward, P. Carpenter, B. Beaudoin, and J. Gridley (2014). Development of new seismological observing capabilities for ice covered environments, *American Geological Union Fall Meeting*, San Francisco, USA.

Boué, P., P. Poli, M. Campillo, H. Pedersen, X. Briand, and P. Roux (2013). Teleseismic correlations of ambient seismic noise for deep global imaging of the Earth, *Geophys. J. Int.,* **194** 844-848.

Busby, R., K. Hafner, and R. Woodward (2013). Transportable Array plans for Alaska and Yukon, *EarthScope National Meeting*, Raleigh, USA.

Castellaro, S., and F. Mulargia (2012). A statistical low noise model of the earth, *Seismol. Res. Lett.*, **83** 39-48.

Cather, S. M. (2002). Preliminary geologic map of the San Antonio 7.5 minute quadrangle, Socorro County, New Mexico. *New Mexico Bureau of Geology and Mineral Resources, Open-File Geologic Map OF-GM-58*, scale 1:24,000.

Crotwell, H. P., T. J. Owens, and J. Ritsema (1999). The TauP Toolkit: Flexible seismic travel-time and ray-path utilities, *Seismol. Res. Lett.*, **70** 154-160.

Custódio, S., N. A. Dias, B. Caldeira, F. Carrilho, S. Carvalho, C. Corela, J. Díaz, J. Narciso, D. Madureira, L. Matias, C. Haberland, and WILAS Team (2014). Ambient noise recorded by a dense broadband seismic deployment in western Iberia, *Bull. Seism. Soc. Am.*, **104** 2985-3007.

Ekström, G., M. Nettles, and A. M. Dziewonski (2012). The global CMT project 2004-2010: Centroid-moment tensors for 13,017 earthquakes, *Phys. Earth Planet. In.,* **200** 1-9.

Esktröm, G., and R. W. Busby (2008). Measurements of seismometer orientation at USArray transportable array and backbone stations, *Seismol. Res. Lett.*, **79** 554-561.

Frassetto, A., B. Busby, K. Hafner, A. Sauter, and R. Woodward (2014). Posthole sensor performance in the USArray Transportable Array – results from testing and initial deployments in Alaska and Canada, *American Geophysical Union Fall Meeting*, San Francisco, CA.

Given, H. K. (1990). Variations in broadband seismic noise at IRIS/IDA stations in the USSR with implications for event detection, *Bull. Seismol. Soc. Am.*, **80** 2072-2088.

Hasselmann, K. (1963). A statistical analysis of the generation of microseisms, *Rev. Geophs.* **1** 177-210.

Kennett, B. L. N., and E. R. Engdahl (1991). Traveltimes for global earthquake location and phase identification, *Geophys. J. Int.*, **105** 429-465.

McNamara, D. E., and R. I. Boaz (2011). PQLX: A seismic data quality control system description, applications and users manual, *U.S. Geological Survey Open-File Report 2010-1292*, 41 p.

McNamara, D. E., C. R. Hutt, R. P. Buland, L. S. Gee, H. Bolton, and H. M Benz (2009). A method to establish seismic noise baselines for automated station assessment, *Seismol. Res. Lett.,* **80** 628-637.

McNamara, D. E., and R. P. Buland (2004). Ambient noise levels in the continental United States, *Bull. Seism. Soc. Am.,* **94** 1517-1527.

National Earthquake Information Center (2013). Global earthquake search. [www.earthquake.usgs.gov/earthquakes/search].

New Mexico Tech Seismological Observatory (2013). Earthquake archives. [www.ees.nmt.edu/outside/NMTSO/archives.html].

Peterson, J. (1993). Observations and modeling of seismic background noise, *U.S. Geological Survey Open-File Report 93-322*, 41 p.

Ringler, A. T., C. R. Hutt, J. R. Evans, and L. D. Sandoval (2011). A comparison of seismic instrument noise coherence analysis techniques, *Bull. Seism. Soc. Am.*, **101** 558-567.

Ringler, A. T., C. R. Hutt, K. Persefield, and L. S. Gee (2013). Seismic stations installation orientation errors at ANSS and IRIS/USGS stations, *Seismol. Res. Lett.*, **84** 926-931.

Sleeman, R., A. van Wettum, and J. Trampert (2006). Three-channel correlation analysis: a new technique to measure instrumental noise of digitizers and seismic sensors, *Bull. Seism. Soc. Am.*, **96**, 258-271.

Sleeman, R., and P. Melichar (2012). PDF representation of the STS-2 self-noise obtained from one year of data recorded in the Conrad Observatory, Austria, *Bull. Seism. Soc. Am.*, **102** 587-597.

Trnkoczy, A., P. Bormann, W. Hanka, L. G. Holcomb, and R. L. Nigbor (2002). Site selection, preparation and installation of seismic stations, in *IASPEI New Manual of Seismological Observatory Practice*, vol. 1, edited by P. Bormann, chap. 7, 1-106, GeoForschungsZentrum, Potsdam.

Welch, P. D. (1967). The use of the fast Fourier transform for the estimation of power spectra: a method based on time averaging over short, modified periodograms, *IEEE Transactions on Audio and Electroacoustics*, **15** 70-73.

Wielandt, E., and T. Forbriger (1999). Near-field seismic displacement and tilt associated with the explosive activity of Stromboli, *Ann. Geofis.*, **42** 407-416.

Wilson, D., J. Leon, R. Aster, J. Ni, J. Schlue, S. Grand, S. Semken, S. Baldridge, and W. Gao (2002). Broadband seismic background noise at temporary seismic stations observed on a regional scale in the southwestern United States, *Bull. Seism. Soc. Am.*, **92** 3335-3341.

List of Figure Captions

Figure 1 a) Cross-section schematic of vault and direct burial emplacement. b) Map view schematic of experimental setup at the installation site, after Anderson et al. (2012).

Figure 2 a) Medians of PDFs for each station from January to August 2012. Vault stations are in darker shades and direct burials are in lighter shades. Dashed lines are the NLNM and NHNM. b) Deviation from the mean of the median noise levels from the four stations over the same time period, with positive values for a higher power than the mean and negatives values for a lower power than the mean.

Figure 3) Daily median noise levels at long periods (20-172 seconds) with respect to the NLNM for eight months of study, 1 January through 31 August 2012, on all four stations. Vertical dashed lines indicate days on which a $M_W \geq 7$ earthquake occurred. Vertical solid lines indicate a mass re-center on Direct Burial 2.

Figure 4) Median probability density functions of hourly MSC for each month between January to August 2012 on the BHE, BHN, and BHZ components of Direct Burial 1 vs. Direct Burial 2, Vault 1 vs. Vault 2 and Direct Burial 1 vs. Vault 1.

Figure 5) Results of MSC analysis of original data and rotated data from the BHE component of Vault 1 during the month of December 2011. a) PDF of magnitude squared coherence of Vault 1 station and Vault 1 station rotated by 20º in the horizontal plane. White lines show median PDF of 1-20º rotations. b) Median probability density functions for 1º, 2º, 3º, 4º, 5º, 10º, and 20º rotations in the horizontal plane. c) PDF of MSC of Vault 1 station and Vault 1 station with 3.2º rotation of the vertical plane. White lines show median PDF of 0.2-3.2º rotations. d) Median PDFs for 0.2º, 0.4º, 0.8º, 1.6º, and 3.2º rotations in the horizontal plane.

Figure 6 a) Hourly integrated and normalized MSC between stations of the same emplacement. Four plots show the hourly MSC between direct burial stations and vault stations on the BHE component for the representative months of January and June at three different frequency bands. The diurnal behavior becomes more apparent in June, along with an overall decrease in coherence in the vault stations. b) Eight months of hourly MSC values recorded on the BHE component converted to the frequency domain. There is a strong diurnal signal on both sets of stations in the long periods, increasing in amplitude through the year. Similar behavior is found on the BHE and BHN components of all other pairings between direct burial and vault stations.

Figure 7) MSC of a M_{W} 7.7 earthquake near Japan on 14 August 2012 recorded on the vertical component with noise windows on the left and signal windows on the right.

Kasey Aderhold
Department of Earth and Environment
Boston University
685 Commonwealth Avenue, Room 130
Boston, MA 02215

Katherine E. Anderson
IRIS PASSCAL Instrument Center
New Mexico Tech
100 East Road
Socorro, NM 87801

Angela M. Reusch
IRIS PASSCAL Instrument Center
New Mexico Tech
100 East Road
Socorro, NM 87801

Mary C. Pfeifer
IRIS PASSCAL Instrument Center
New Mexico Tech
100 East Road
Socorro, NM 87801

Richard C. Aster
Geosciences Department
322E NR Building
Warner College of Natural Resources
Colorado State University
Fort Collins, CO 80523

Tim Parker
IRIS PASSCAL Instrument Center
New Mexico Tech
100 East Road
Socorro, NM 87801

a)

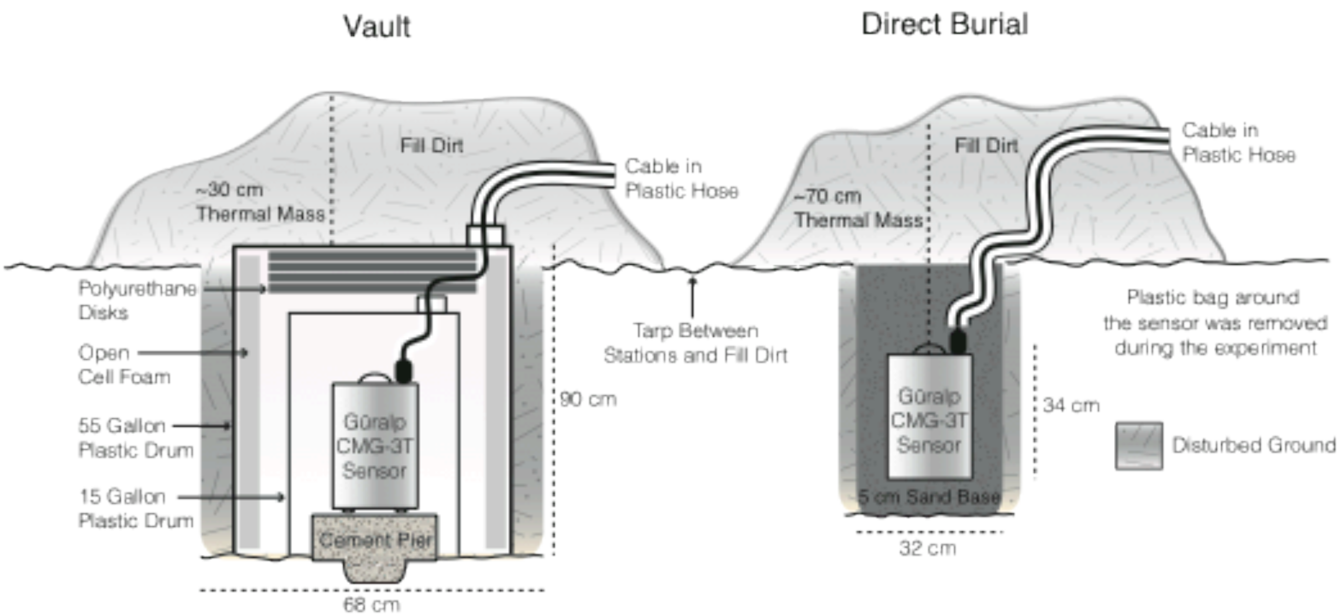

b)

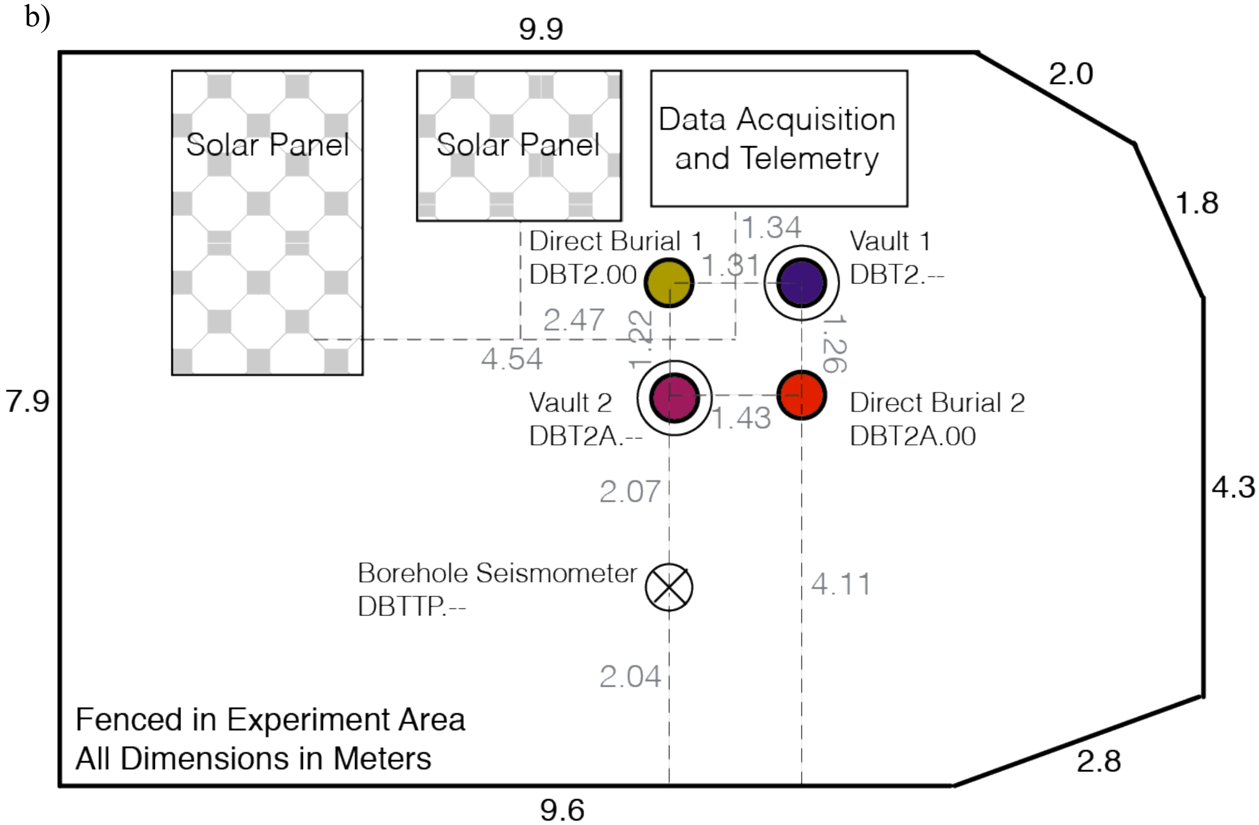

Figure 1 a) Cross-section schematic of vault and direct burial emplacement, after Anderson et al. (2012). b) Map view schematic of experimental setup at the installation site, after Anderson et al. (2012).

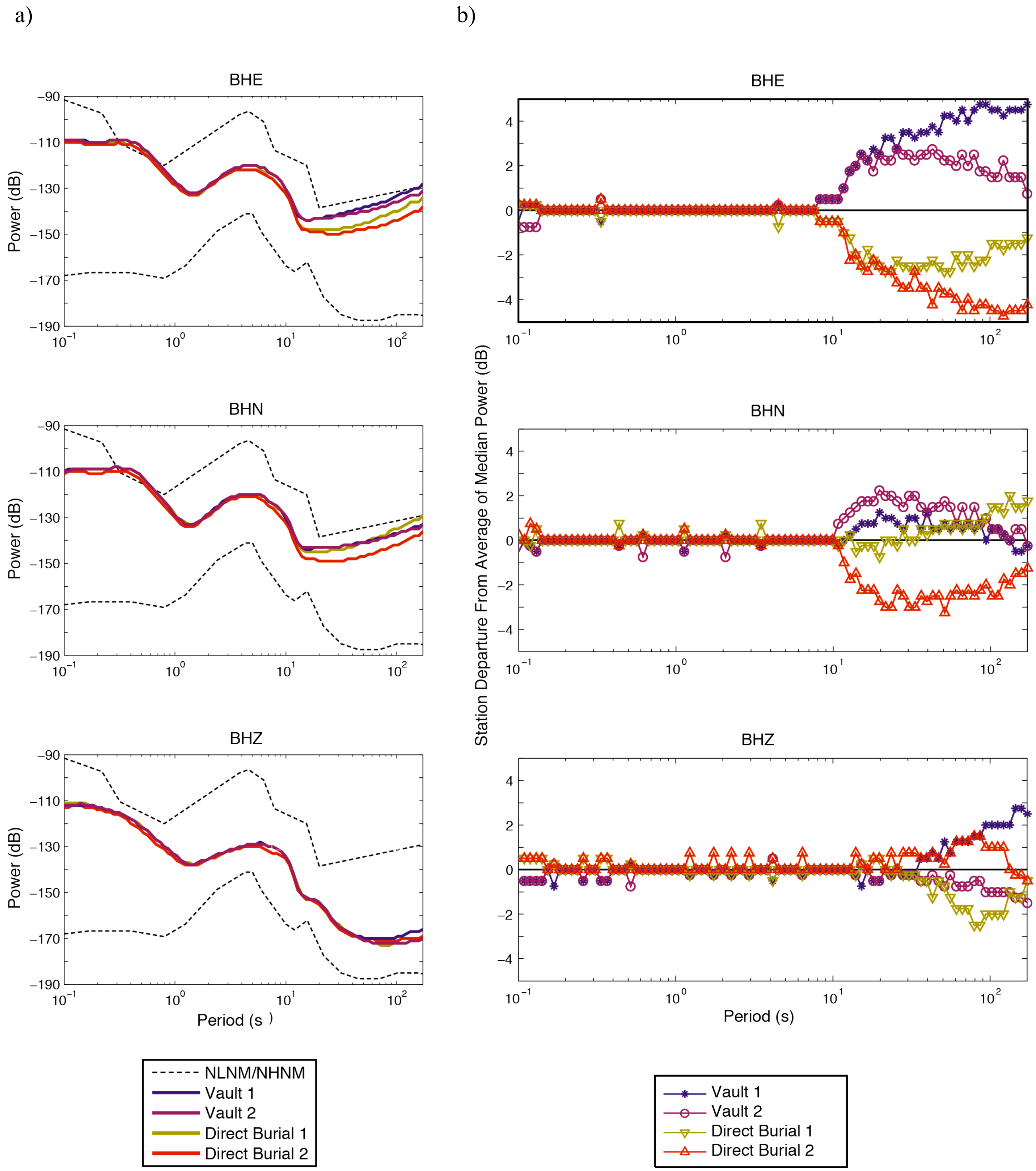

Figure 2 a) Medians of PDFs for each station from January to August 2012. Vault stations are in darker shades and direct burials are in lighter shades. Dashed lines are the NLNM and NHNM. b) Deviation from the mean of the median noise levels from the four stations over the same time period, with positive values for a higher power than the mean and negatives values for a lower power than the mean.

Figure 3

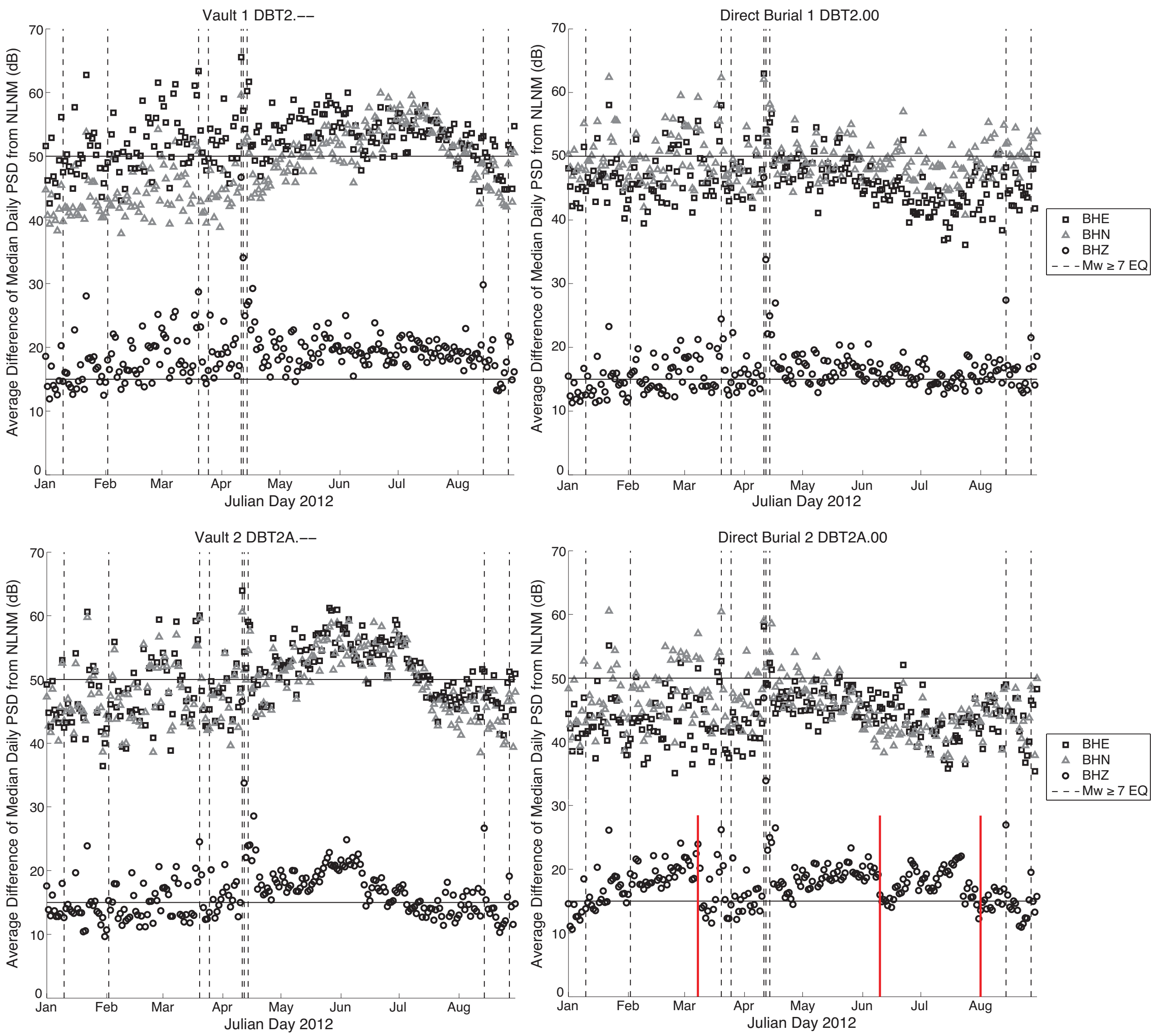

Figure 3) Daily median noise levels at long periods (20-172 seconds) with respect to the NLNM for eight months of study, 1 January through 31 August 2012, on all four stations. Vertical dashed lines indicate days on which a $M_W \geq 7$ earthquake occurred. Vertical solid lines indicate a mass re-center on Direct Burial 2.

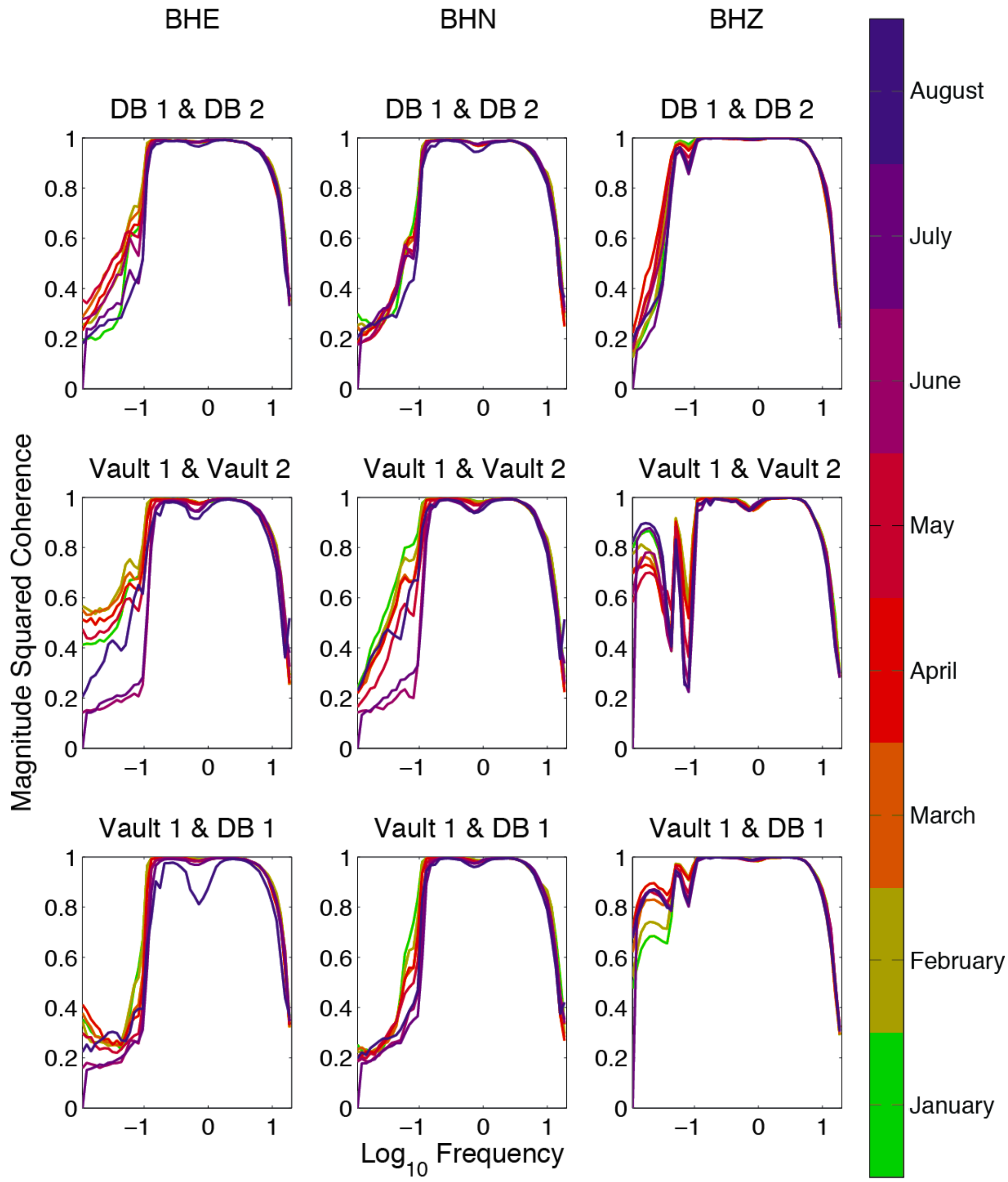

Figure 4) Median probability density functions of hourly MSC for each month between January to August 2012 on the BHE, BHN, and BHZ components of Direct Burial 1 vs. Direct Burial 2, Vault 1 vs. Vault 2 and Direct Burial 1 vs. Vault 1.

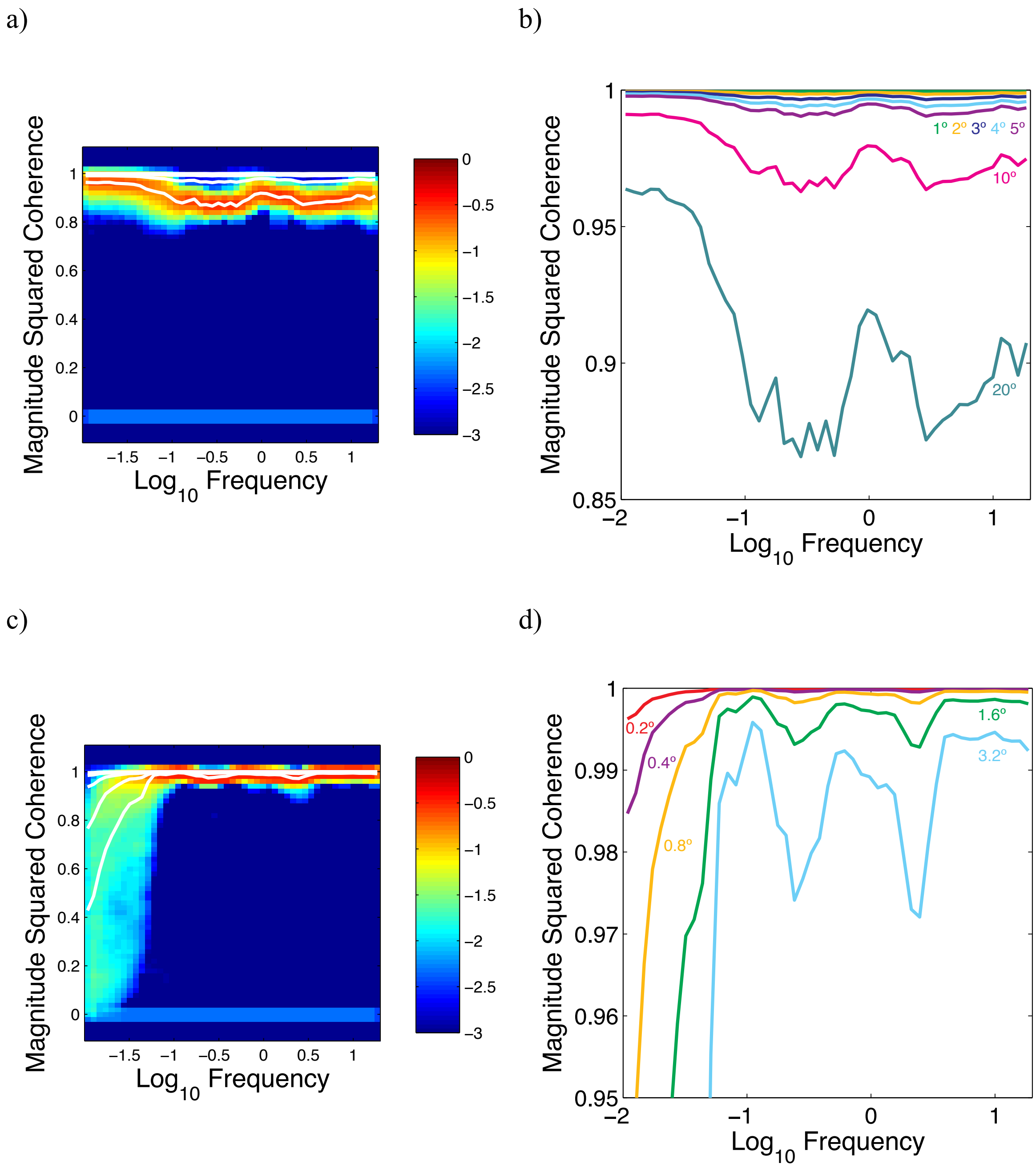

Figure 5) Results of MSC analysis of original data and rotated data from the BHE component of Vault 1 during the month of December 2011. a) PDF of magnitude squared coherence of Vault 1 station and Vault 1 station rotated by 20º in the horizontal plane. White lines show median PDF of 1-20º rotations. b) Median probability density functions for 1º, 2º, 3º, 4º, 5º, 10º, and 20º rotations in the horizontal plane. c) PDF of MSC of Vault 1 station and Vault 1 station with 3.2º rotation of the vertical plane. White lines show median PDF of 0.2-3.2º rotations. d) Median PDFs for 0.2º, 0.4º, 0.8º, 1.6º, and 3.2º rotations in the horizontal plane.

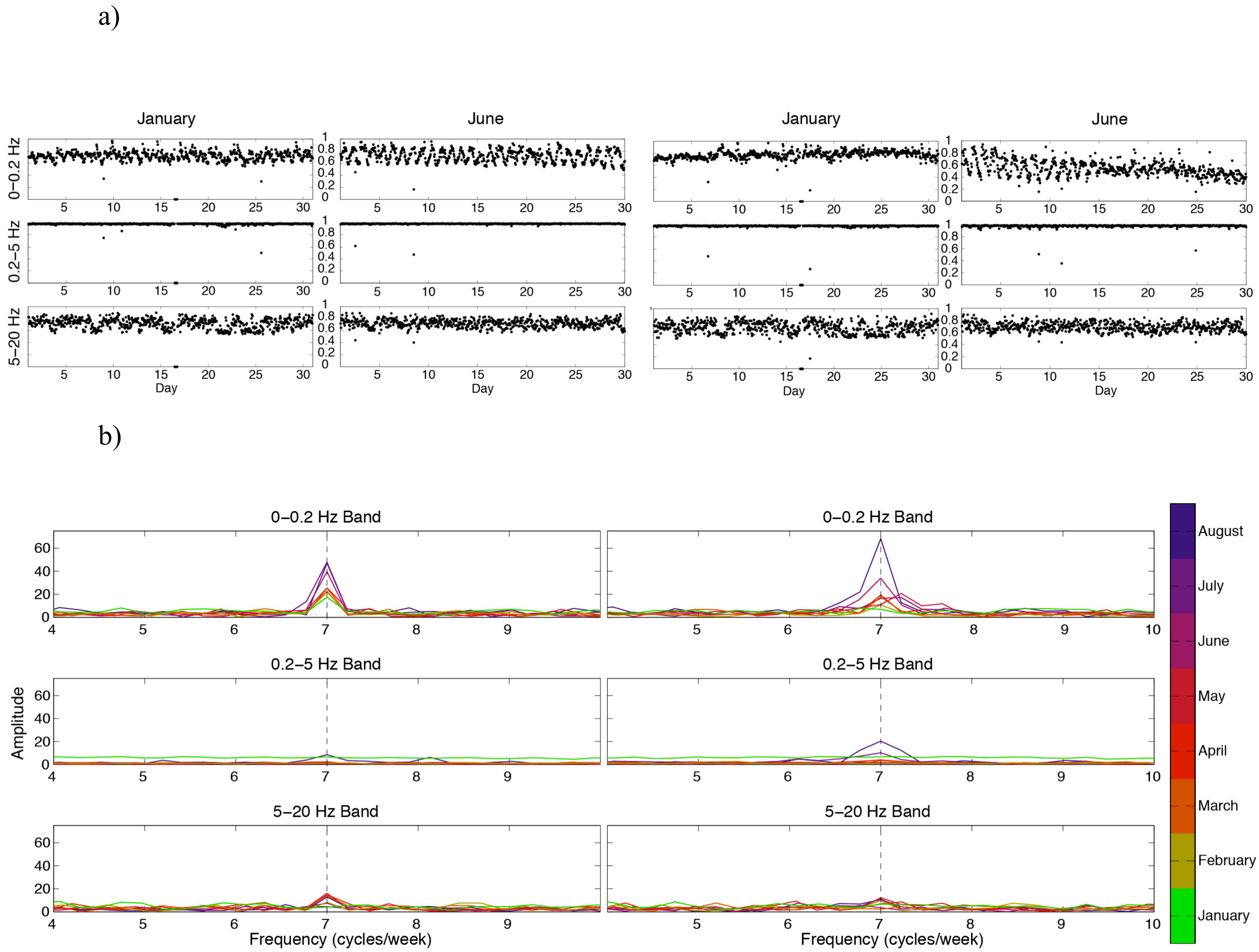

Figure 6 a) Hourly integrated and normalized MSC between stations of the same emplacement. Four plots show the hourly MSC between direct burial stations and vault stations on the BHE component for the representative months of January and June at three different frequency bands. The diurnal behavior becomes more apparent in June, along with an overall decrease in coherence in the vault stations. b) Eight months of hourly MSC values recorded on the BHE component converted to the frequency domain. There is a strong diurnal signal on both sets of stations in the long periods, increasing in amplitude through the year. Similar behavior is found on the BHE and BHN components of all other pairings between direct burial and vault stations.

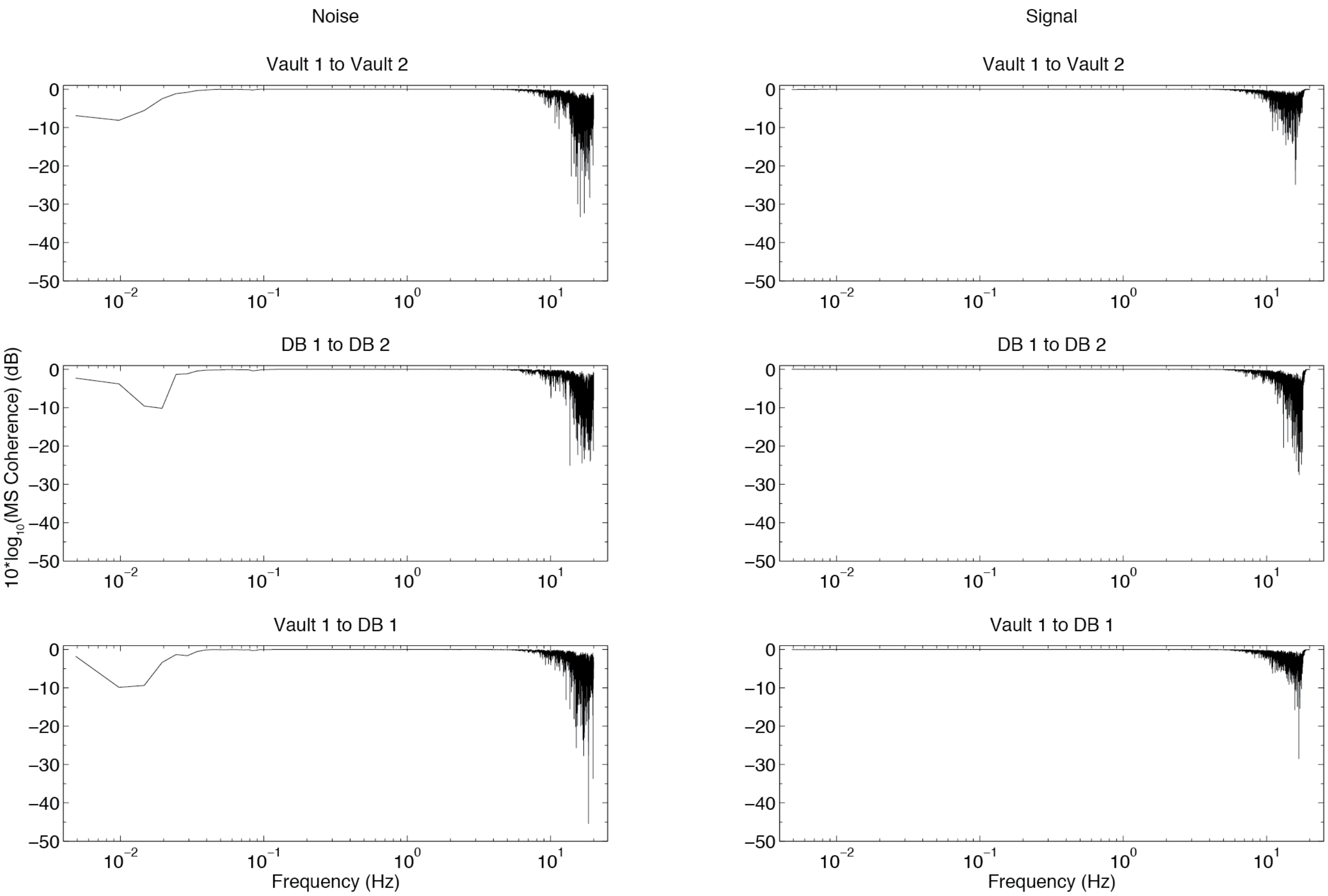

Figure 7) MSC of a M_W 7.7 earthquake near Japan on 14 August 2012 recorded on the vertical component with noise windows on the left and signal windows on the right.

Table 1) Station abbreviations used in the paper and their attributes during the experiment.

Station Name	Station Code	Thickness of Thermal Mass	Failure	Evidence of Water
Vault 1	DBT2.--	30 cm	None	10-13 cm mark on pier
Vault 2	DBT2A.--	30 cm	None	10 cm mark on pier
Direct Burial 1	DBT2.00	60 cm	11/18/12	Water in cable housing
Direct Burial 2	DBT2A.00	76 cm	9/22/12	None

Table 2) Signal-to-noise ratios for all 23 M_W≥6.0 earthquakes at distances of 30º to 90º from the stations.[1,2]

	1/23 6.1	1/30 6.4	3/5 6.1	3/14 6.9	3/14 6.1	3/25 7.1	4/17 6.7	5/14 6.2	5/25 6.1	5/28 6.7	6/4 6.3	6/4 6.3	6/7 6.0	6/7 6.1	6/19 6.0	6/24 6.0	7/8 6.0	7/20 6.0	8/2 6.1	8/10 6.2	8/14 7.7	8/27 7.3	8/30 6.8	Mean	Median
V1	6.7	29.8	6.9	50.1	10.0	19.8	13.4	18.3	12.9	5.8	38.7	22.0	5.4	27.3	26.3	21.5	9.8	6.8	12.4	26.1	191.3	33.6	12.2	26.4	18.3
V2	6.6	29.8	6.8	50.2	9.9	19.4	13.4	17.8	12.9	5.7	38.8	21.9	5.3	27.3	26.3	21.5	9.7	6.8	12.4	25.9	189.4	33.2	12.3	26.2	17.8
DB1	6.7	29.7	6.9	50.0	10.0	17.7	13.6	18.4	12.8	5.8	38.9	22.2	5.4	26.7	26.0	21.5	9.7	6.8	12.4	25.8	191.7	33.6	12.4	26.3	17.7
DB2	6.6	29.7	6.9	49.9	10.0	17.2	13.5	18.0	13.1	5.8	39.0	21.9	5.4	27.4	26.4	21.6	9.7	6.8	12.4	25.9	189.0	33.5	12.3	26.2	17.2

[1] The date of the earthquake is on top with the moment magnitude (M_W) on the bottom.

[2] V1 and V2 stand for Vault 1 and Vault 2. DB1 and DB2 stand for Direct Burial 1 and Direct Burial 2.

Table 3) Signal-to-noise ratios for six 1.1 ≥ M_L ≥ 0.1 earthquakes at distances within 10 km from the stations.[1,2]

	4/26 0.3	5/3 0.2	6/4 0.7	6/4 1.1	6/10 0.9	8/04 0.1	Mean	Median
V1	3.179	2.03	1.81	1.72	2.66	2.59	2.33	2.31
V2	3.226	1.97	1.73	1.76	2.59	2.56	2.31	2.26
DB1	3.481	2.05	1.92	1.81	2.83	2.77	2.48	2.41
DB2	3.228	2.12	1.98	1.83	2.89	2.77	2.47	2.44

[1] The date of the earthquake is on top with the local magnitude from the New Mexico Tech Seismological Observatory (M_L) on the bottom.

[2] V1 and V2 stand for Vault 1 and Vault 2. DB1 and DB2 stand for Direct Burial 1 and Direct Burial 2.

Data quality of co-located portable broadband seismometers using direct burial and vault emplacement

Kasey Aderhold, Katherine E. Anderson, Angela M. Reusch, Mary C. Pfeifer, Richard Aster, and Tim Parker

Electronic Supplement:

The supplementary material for this paper contains figures of the daily median noise levels in the microseism band, monthly probability density functions for the magnitude squared coherence between the six station couplings (Direct Burial 1 to Direct Burial 2, Vault 1 to Direct Burial 1, Vault 1 to Direct Burial 2, Vault 1 to Vault 2, Vault 2 to Direct Burial 1, Vault 2 to Direct Burial 2) for all three components (BHE, BHN, BHZ), results of the coherency self-noise analysis, and the recordings of the teleseismic and local earthquakes used for the signal-to-noise analysis.

Figure S1) Daily median noise levels on the microseism band (2-20 seconds) with respect to the NLNM for eight months of study, 1 January through 31 August 2012, on all four stations. Vertical dashed lines indicate days on which a $M_W \geq 7$ earthquake occurred.

Figure S2) Probability density function of magnitude squared coherence on the BHZ component. Probability density function is taken of the hourly magnitude squared coherences for each month from January to August 2012 for each of the six station pairings (First column from top to bottom: Direct Burial 1 to Direct Burial 2, Vault 1 to Direct Burial 1, Vault 1 to Direct Burial 2; second column from top to bottom: Vault 1 to Vault 2, Vault 2 to Direct Burial 1, Vault 2 to

Direct Burial 2). The x-axis is the $\log_{10}$ of frequency, the y-axis is magnitude squared coherence, and the black line is the median of the PDF.

Figure S3) Probability density function of magnitude squared coherence on the BHE component. Probability density function is taken of the hourly magnitude squared coherences for each month from January to August 2012 for each of the six station pairings (First column from top to bottom: Direct Burial 1 to Direct Burial 2, Vault 1 to Direct Burial 1, Vault 1 to Direct Burial 2; second column from top to bottom: Vault 1 to Vault 2, Vault 2 to Direct Burial 1, Vault 2 to Direct Burial 2). The x-axis is the $\log_{10}$ of frequency, the y-axis is magnitude squared coherence, and the black line is the median of the PDF.

Figure S4) Probability density function of magnitude squared coherence on the BHN component. Probability density function is taken of the hourly magnitude squared coherences for each month from January to August 2012 for each of the six station pairings (First column from top to bottom: Direct Burial 1 to Direct Burial 2, Vault 1 to Direct Burial 1, Vault 1 to Direct Burial 2; second column from top to bottom: Vault 1 to Vault 2, Vault 2 to Direct Burial 1, Vault 2 to Direct Burial 2). The x-axis is the $\log_{10}$ of frequency, the y-axis is magnitude squared coherence, and the black line is the median of the PDF.

Figure S5) Results from horizontal rotations in the North-East plane relative to Vault 1 to correct for orientation errors using recorded data from the entire month of December 2011. Rotations were 3.1º for Direct Burial 1, -2.4º for Direct Burial 2, and -4.4º for Vault 2 clockwise from north. Median PSDs of all noise are in solid lines and median PSDs of uncorrelated installation/instrument noise are in dashed lines.

Figure S6) Results from dip and azimuth vertical rotation for the four stations to correct for nonparallel vertical components using recorded data from the entire month of December 2011. Rotations were 0.2º/10º for Vault 1, 0.35º/175º for Vault 2, 0.4º/20º for Direct Burial 1, and 0.3º/125º for Direct Burial 2 for dip and azimuth (clockwise from north) respectively. Median PSDs of all noise are in solid lines and median PSDs of uncorrelated installation/instrument noise are in dashed lines.

Figure S7) a) Normalized and band-pass filtered teleseismic seismograms on BHZ component at the four stations for all 23 $M_W \geq 6.0$ earthquakes between 30º and 90º distance from the study site. The black vertical line shows the *P* arrival picks with the noise window to the left and the signal window to the right, and date of the event on the bottom left. b) Map of gCMT (Esktröm et al., 2012) moment tensors for earthquake of $M_W \geq 6.0$ from January to August 2012. Black mechanisms were used for the signal to noise calculations and grey were not.

Figure S8) Normalized and high-pass filtered seismograms for the six $1.1 \geq M_L \geq 0.1$ local earthquakes recorded on the four stations. The handpicked first arrival is indicated by the solid line and the 1 second noise and signal windows are shown with the dashed lines. The date of the event is indicated in the lower left corner. For magnitudes, refer to Table 3 in the paper.

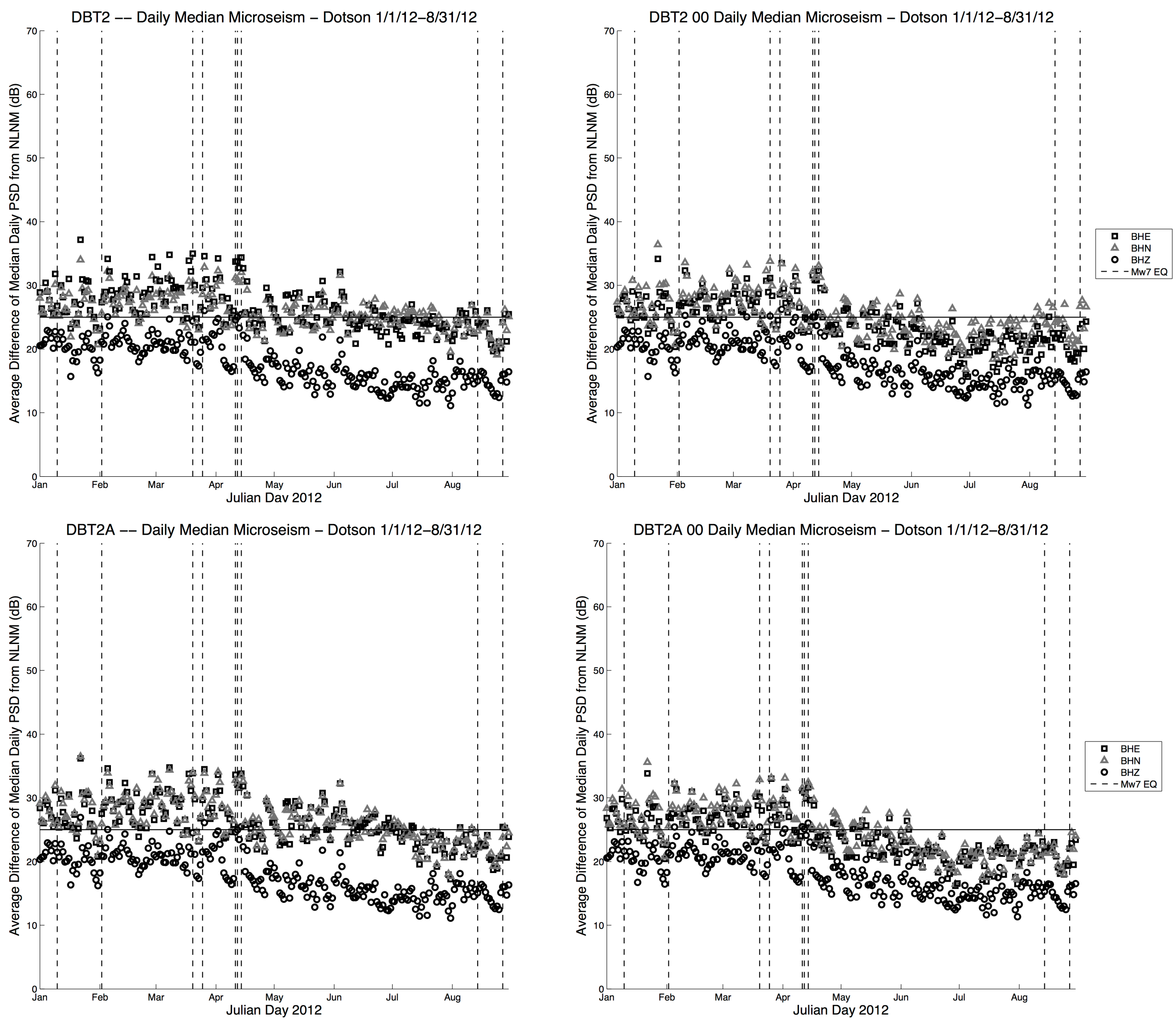
DBT2 -- Daily Median Microseism - Dotson 1/1/12-8/31/12
DBT2 00 Daily Median Microseism - Dotson 1/1/12-8/31/12
DBT2A -- Daily Median Microseism - Dotson 1/1/12-8/31/12
DBT2A 00 Daily Median Microseism - Dotson 1/1/12-8/31/12
Average Difference of Median Daily PSD from NLNM (dB)
Julian Day 2012
Jan
Feb
Mar
Apr
May
Jun
Jul
Aug
BHE
BHN
BHZ
Mw7 EQ

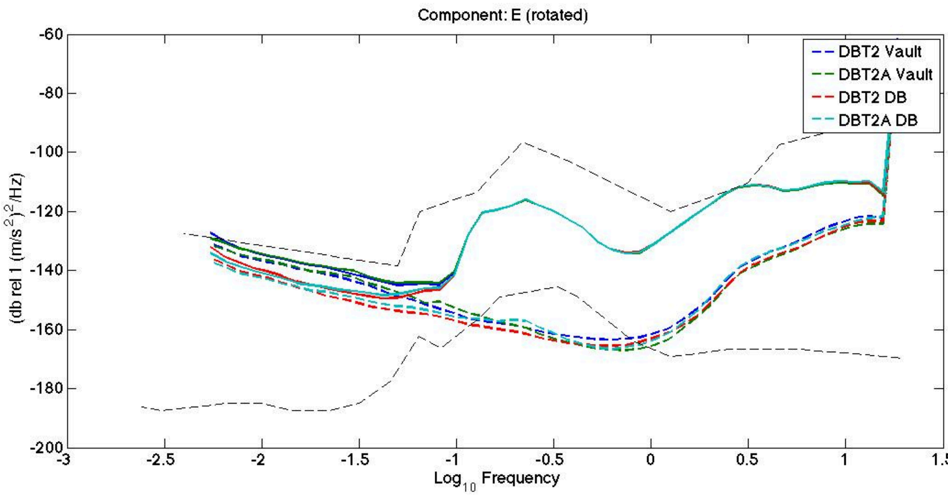
Component: E (rotated)
(db rel 1 (m/s^2)^2/Hz)
Log10 Frequency
DBT2 Vault
DBT2A Vault
DBT2 DB
DBT2A DB

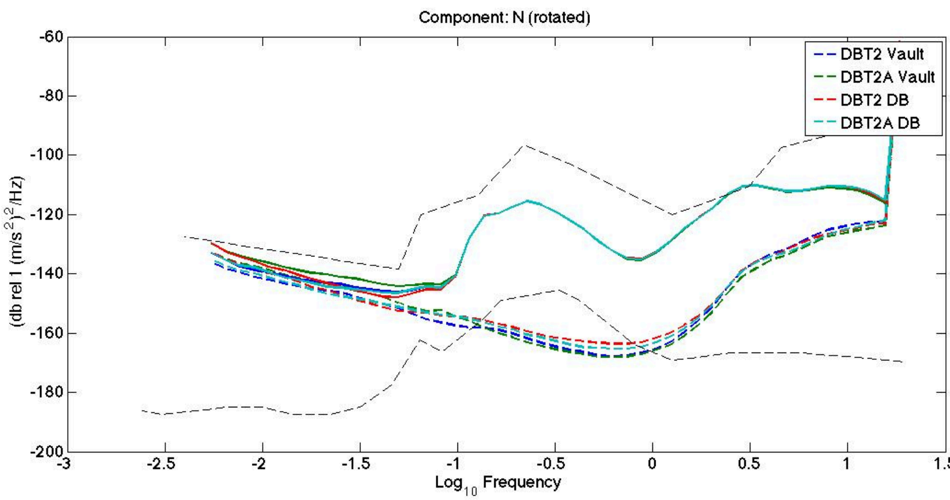
Component: N (rotated)
(db rel 1 (m/s^2)^2/Hz)
Log10 Frequency
DBT2 Vault
DBT2A Vault
DBT2 DB
DBT2A DB

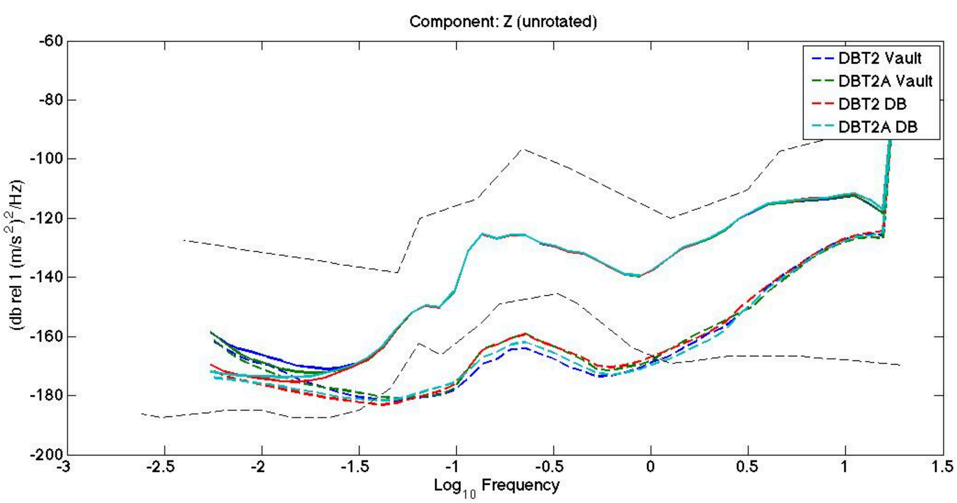
Component: Z (unrotated)
(db rel 1 (m/s^2)^2/Hz)
Log10 Frequency
DBT2 Vault
DBT2A Vault
DBT2 DB
DBT2A DB

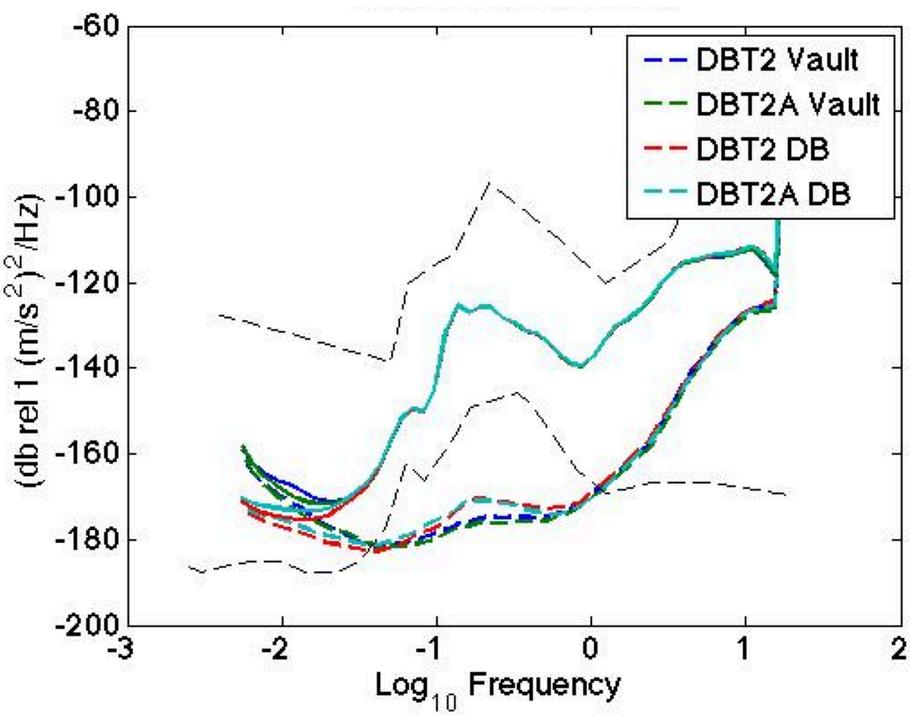
DBT2 Vault
DBT2A Vault
DBT2 DB
DBT2A DB
-60
-80
-100
-120
-140
-160
-180
-200
-3
-2
-1
0
1
2
(db rel 1 (m/s^2)^2/Hz)
Log$_{10}$ Frequency

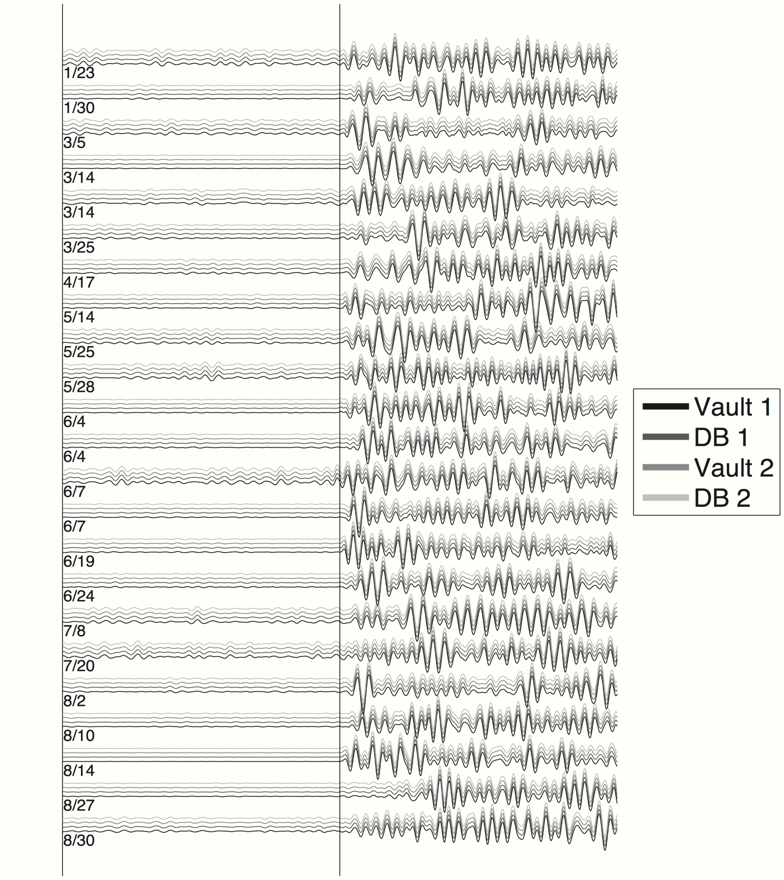
1/23
1/30
3/5
3/14
3/14
3/25
4/17
5/14
5/25
5/28
6/4
6/4
6/7
6/7
6/19
6/24
7/8
7/20
8/2
8/10
8/14
8/27
8/30
Vault 1
DB 1
Vault 2
DB 2

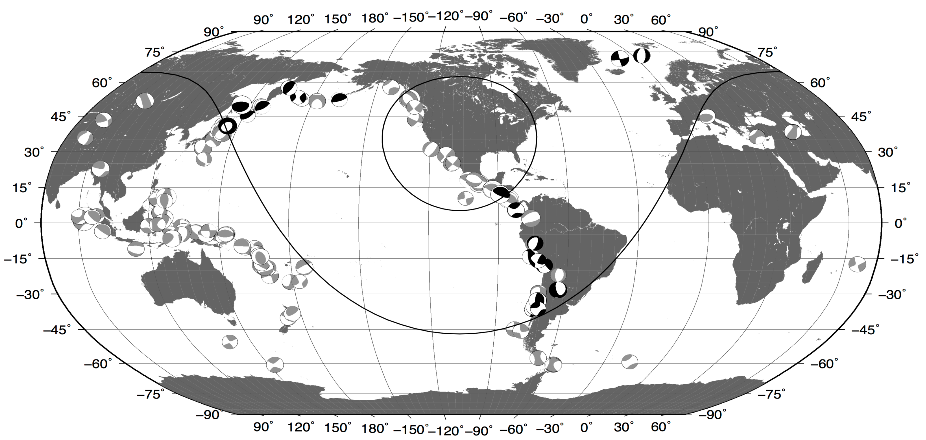
90° 120° 150° 180° −150° −120° −90° −60° −30° 0° 30° 60°
90°
75°
60°
45°
30°
15°
0°
−15°
−30°
−45°
−60°
−75°
−90°

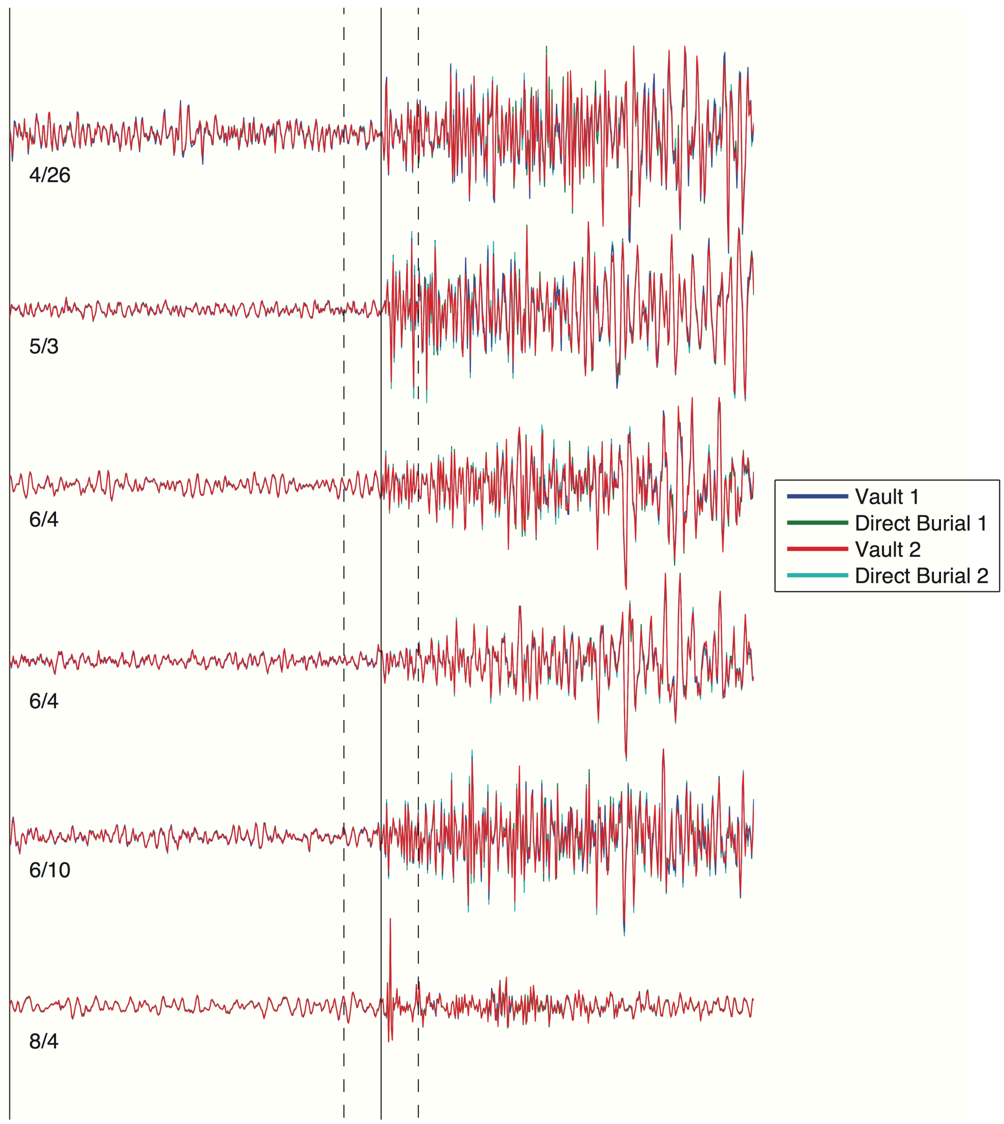
4/26
5/3
6/4
6/4
6/10
8/4
Vault 1
Direct Burial 1
Vault 2
Direct Burial 2

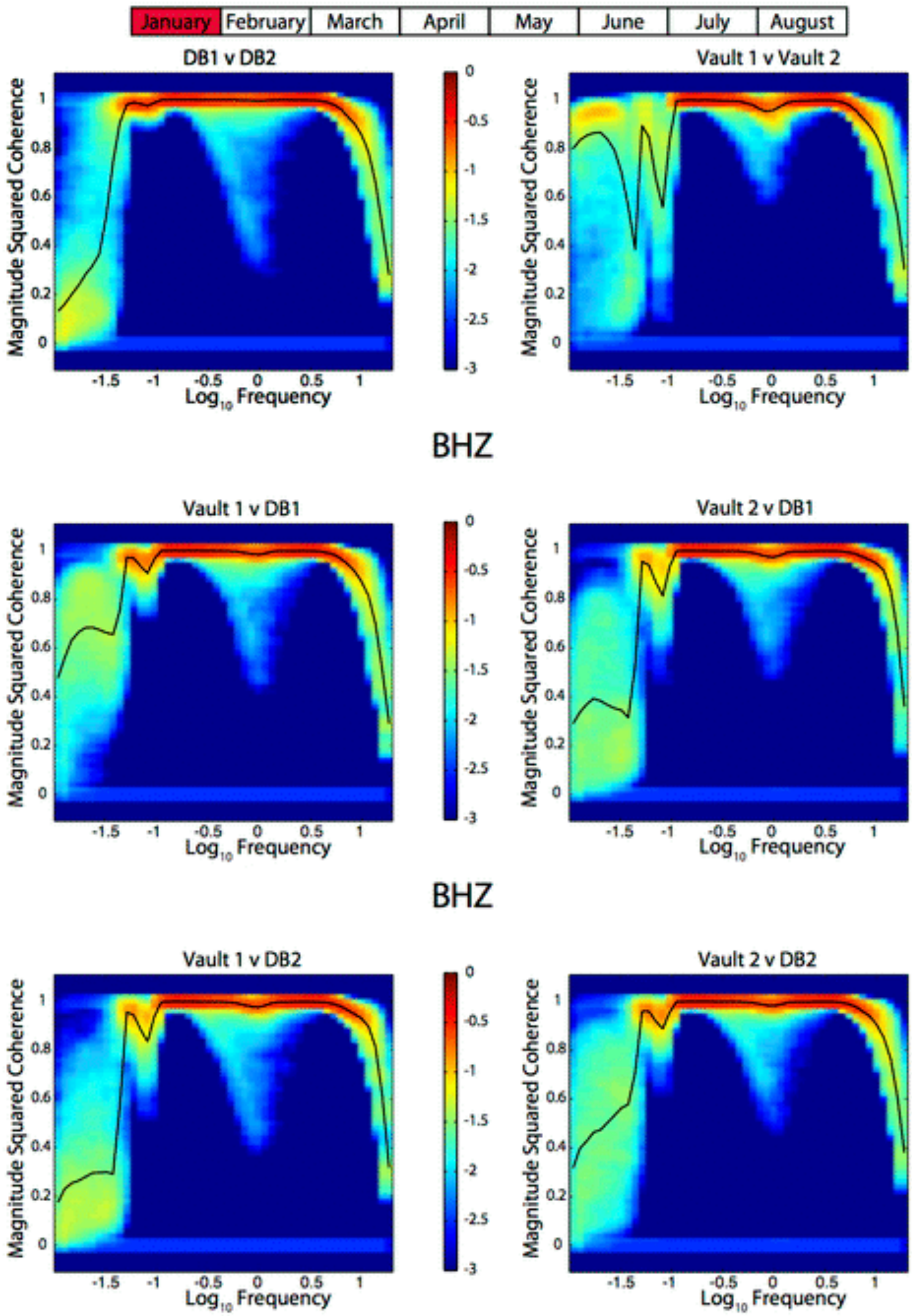
January
February
March
April
May
June
July
August
DB1 v DB2
Vault 1 v Vault 2
BHZ
Vault 1 v DB1
Vault 2 v DB1
BHZ
Vault 1 v DB2
Vault 2 v DB2
Magnitude Squared Coherence
Log10 Frequency
-1.5
-1
-0.5
0
0.5
1
0.2
0.4
0.6
0.8
-2
-2.5
-3

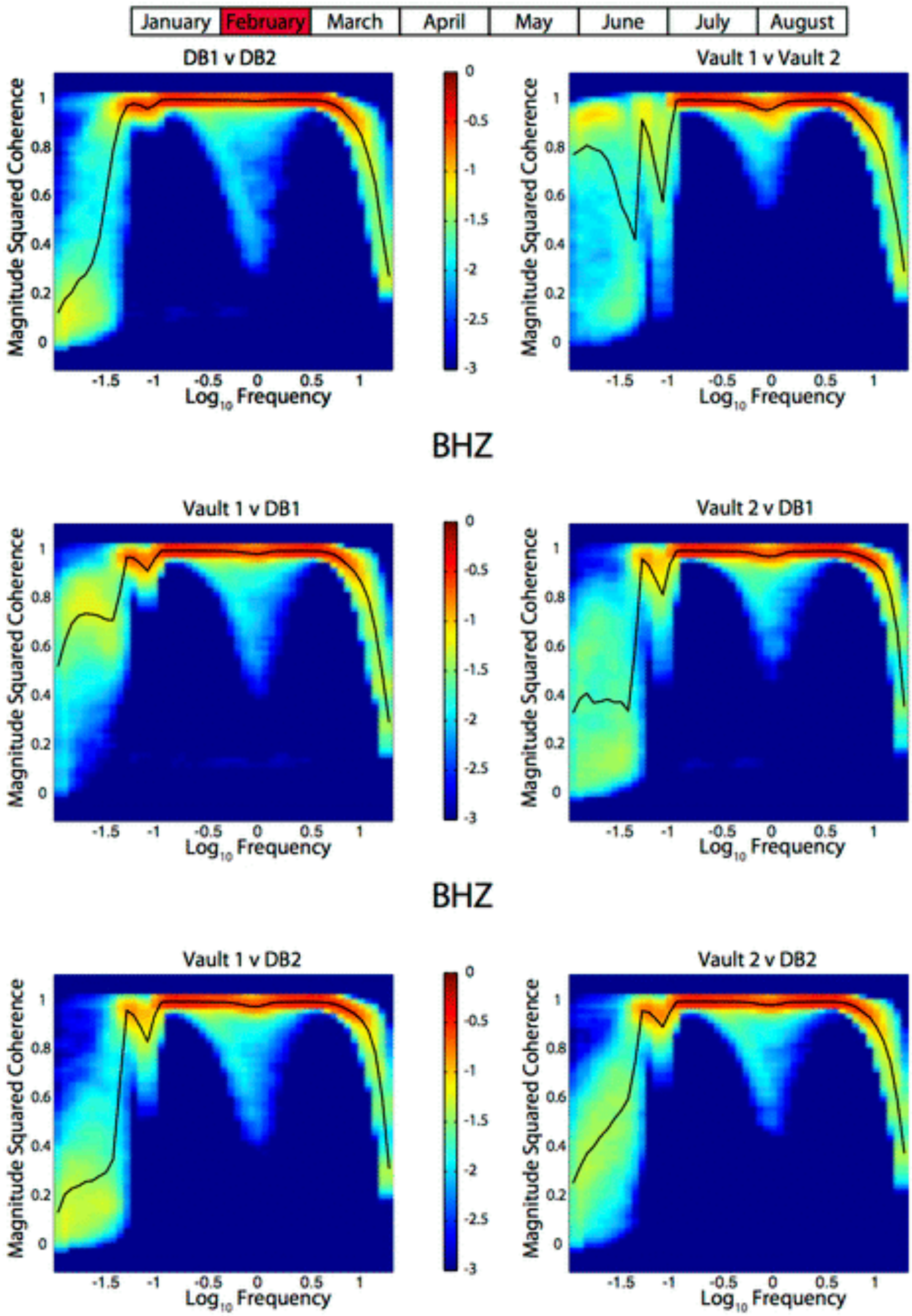
January
February
March
April
May
June
July
August
DB1 v DB2
Vault 1 v Vault 2
BHZ
Vault 1 v DB1
Vault 2 v DB1
BHZ
Vault 1 v DB2
Vault 2 v DB2
Magnitude Squared Coherence
Log10 Frequency

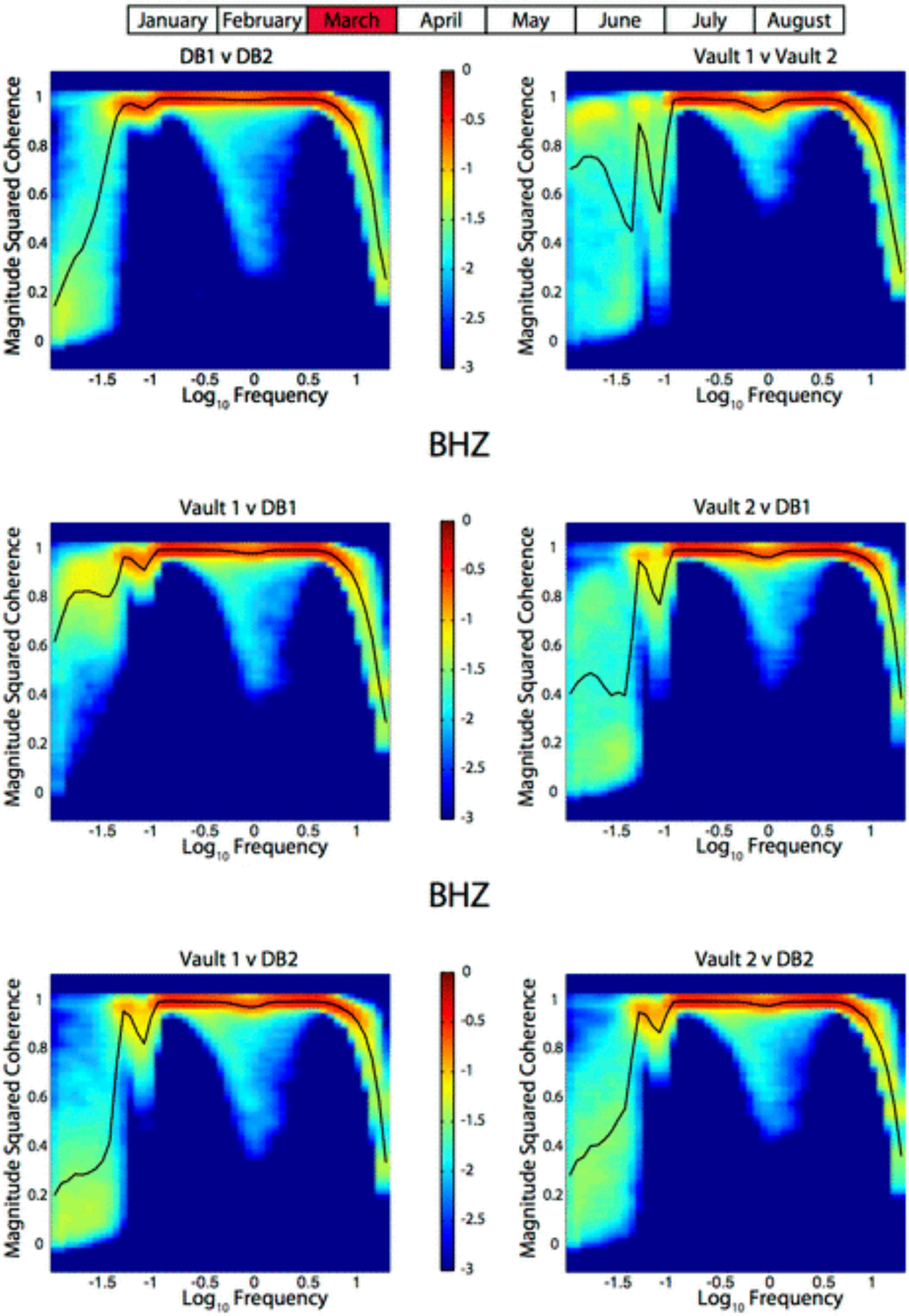
January
February
March
April
May
June
July
August
DB1 v DB2
Vault 1 v Vault 2
BHZ
Vault 1 v DB1
Vault 2 v DB1
BHZ
Vault 1 v DB2
Vault 2 v DB2
Magnitude Squared Coherence
Log10 Frequency
-1.5
-1
-0.5
0
0.5
1
0
0.2
0.4
0.6
0.8
1
-3
-2.5
-2
-1.5
-1
-0.5
0

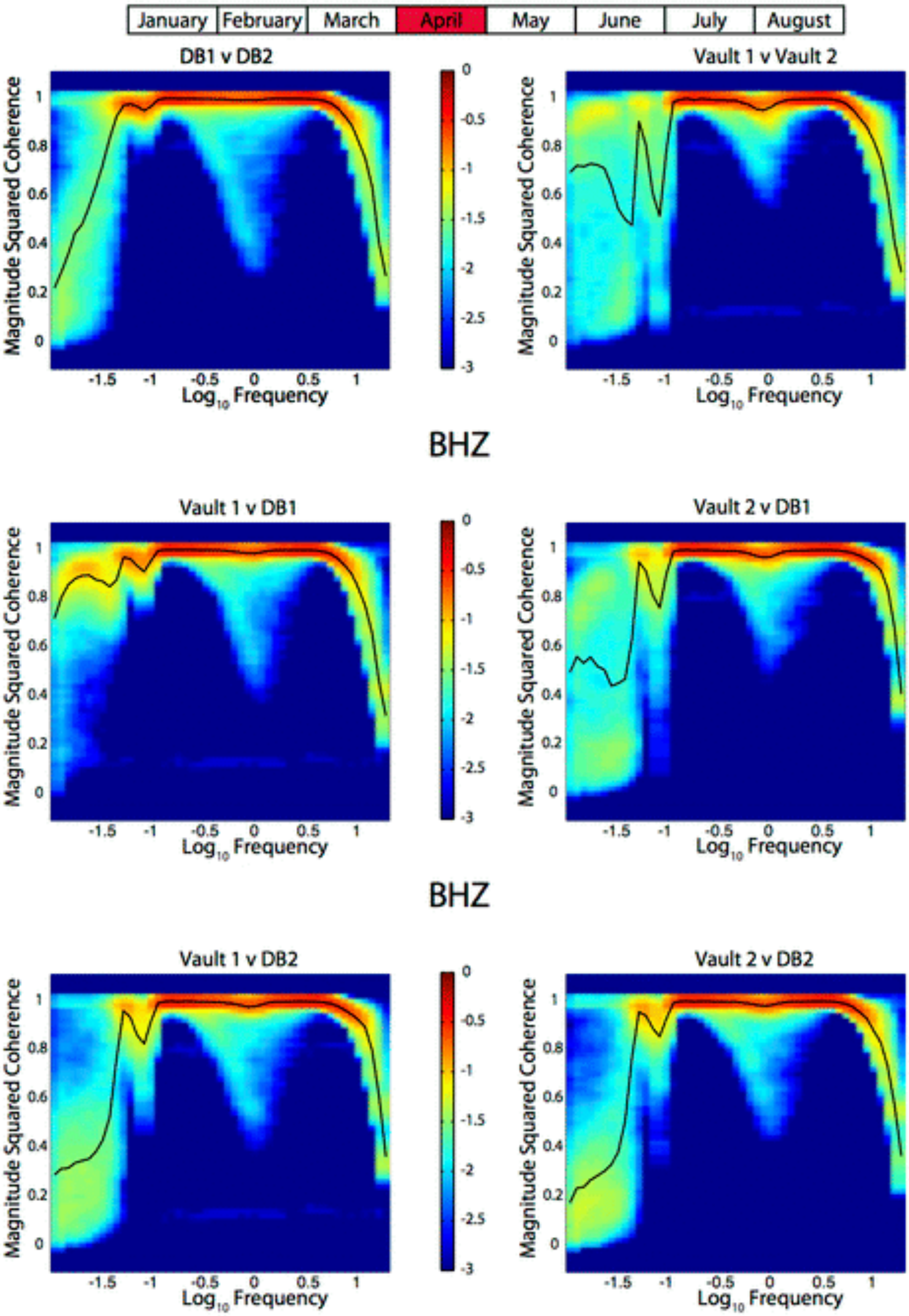

January
February
March
April
May
June
July
August
DB1 v DB2
Vault 1 v Vault 2
BHZ
Vault 1 v DB1
Vault 2 v DB1
BHZ
Vault 1 v DB2
Vault 2 v DB2
Magnitude Squared Coherence
Log10 Frequency

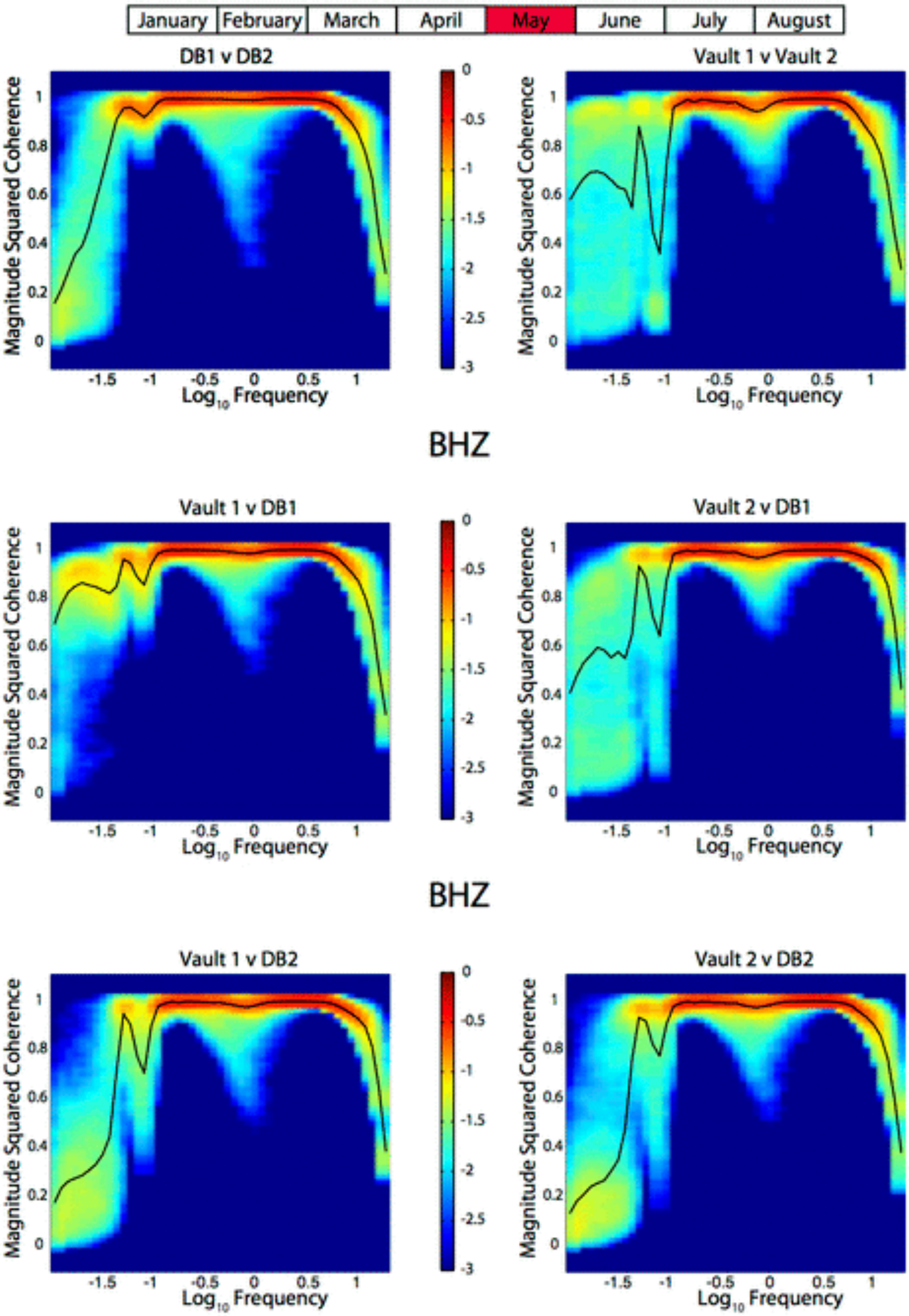

January
February
March
April
May
June
July
August
DB1 v DB2
Vault 1 v Vault 2
BHZ
Vault 1 v DB1
Vault 2 v DB1
BHZ
Vault 1 v DB2
Vault 2 v DB2
Magnitude Squared Coherence
Log_{10} Frequency

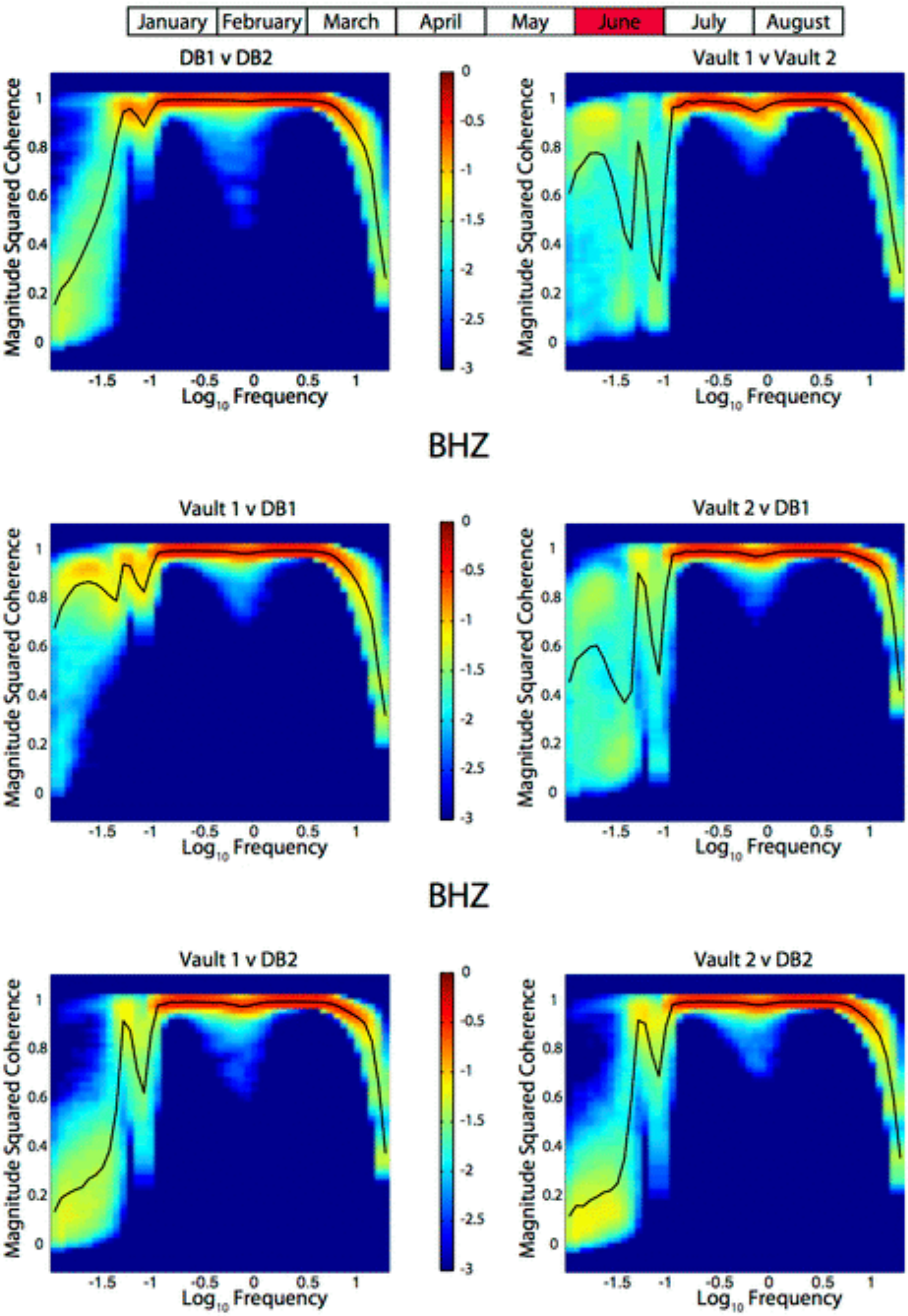
January
February
March
April
May
June
July
August
DB1 v DB2
Vault 1 v Vault 2
BHZ
Vault 1 v DB1
Vault 2 v DB1
BHZ
Vault 1 v DB2
Vault 2 v DB2
Magnitude Squared Coherence
Log_{10} Frequency
0
-0.5
-1
-1.5
-2
-2.5
-3

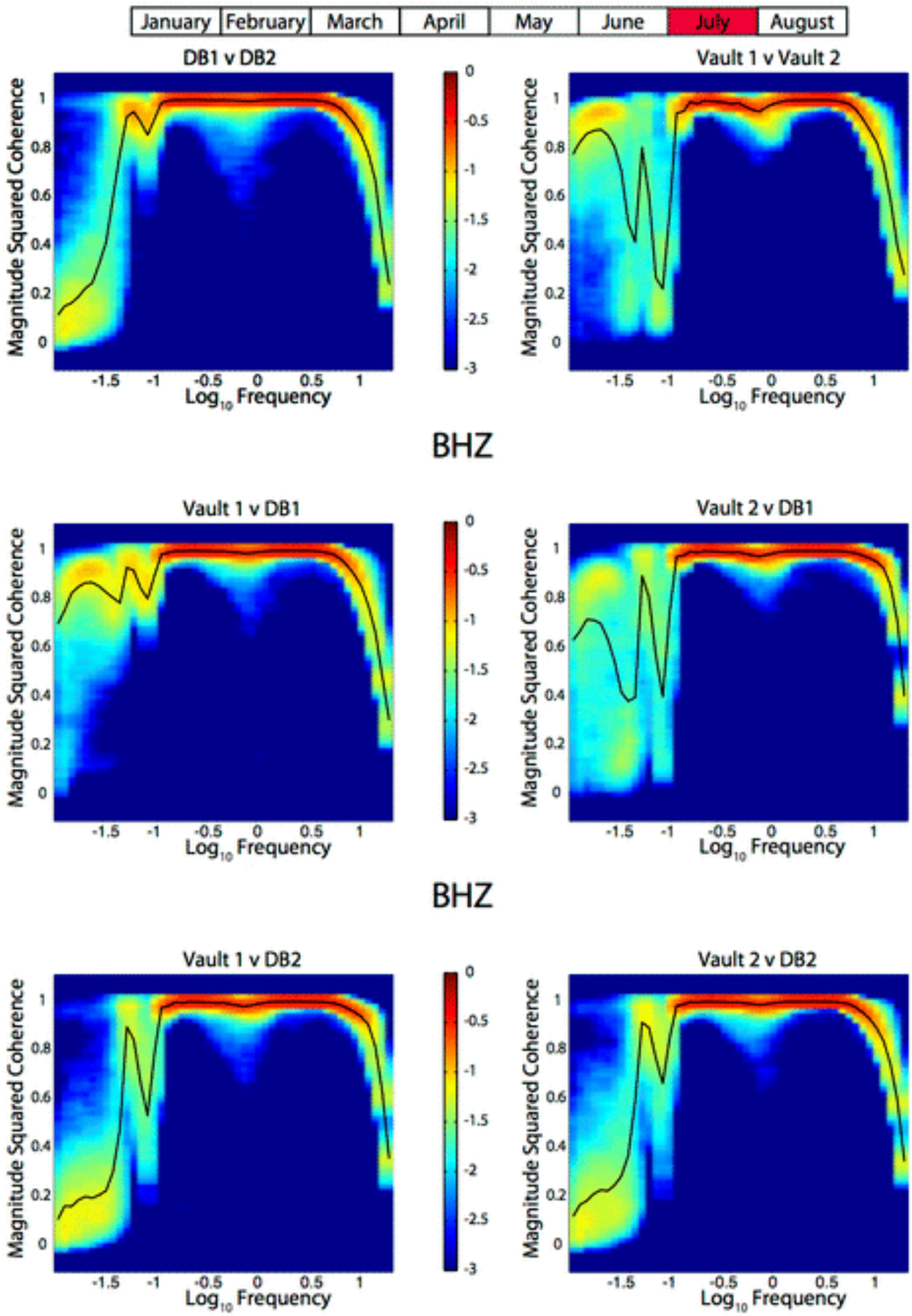
January
February
March
April
May
June
July
August
DB1 v DB2
Vault 1 v Vault 2
BHZ
Vault 1 v DB1
Vault 2 v DB1
BHZ
Vault 1 v DB2
Vault 2 v DB2
Magnitude Squared Coherence
Log10 Frequency

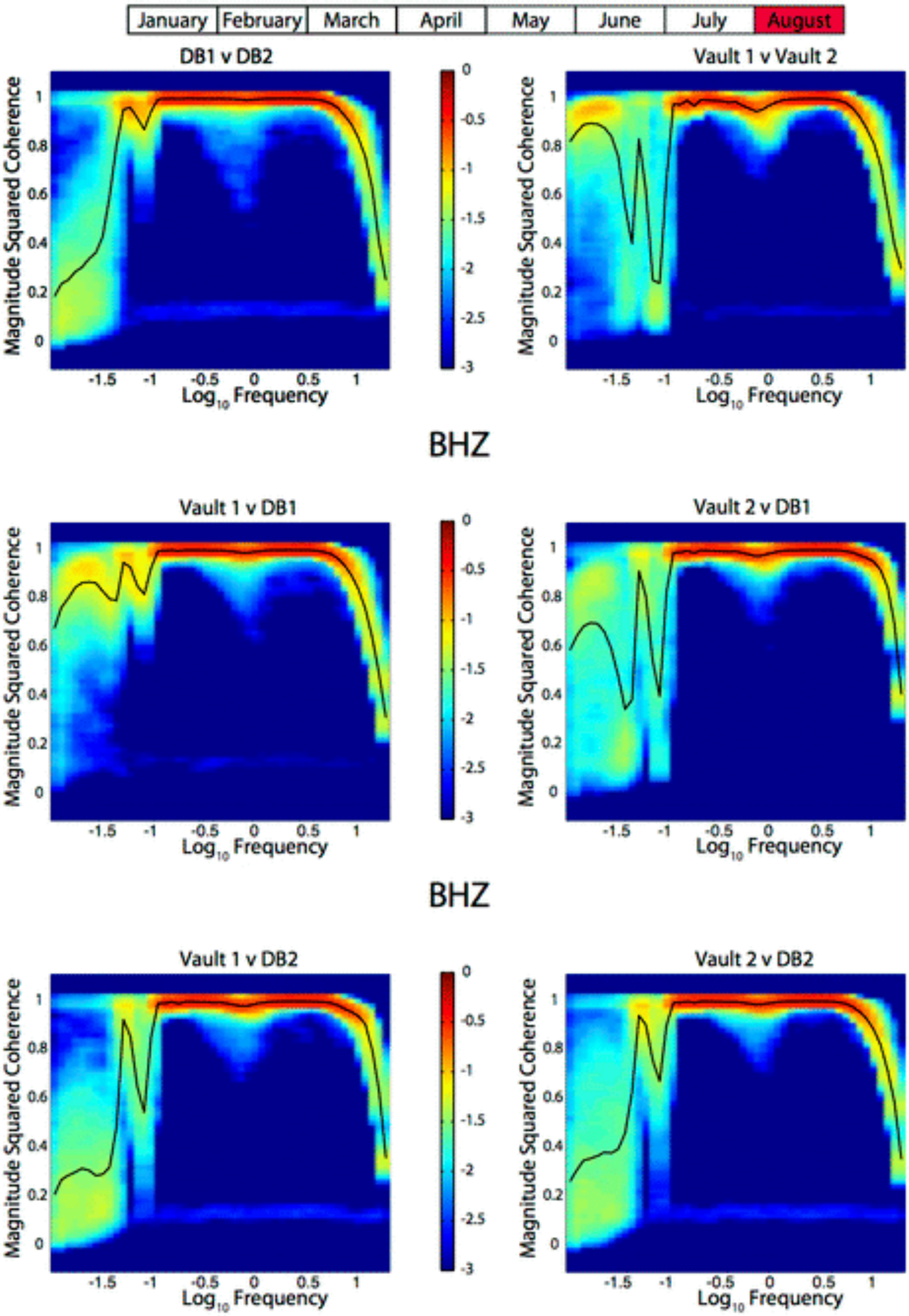
January
February
March
April
May
June
July
August
DB1 v DB2
Vault 1 v Vault 2
Vault 1 v DB1
Vault 2 v DB1
Vault 1 v DB2
Vault 2 v DB2
BHZ
BHZ
Magnitude Squared Coherence
Log10 Frequency
0
0.2
0.4
0.6
0.8
1
-1.5
-1
-0.5
0
0.5
1
0
-0.5
-1
-1.5
-2
-2.5
-3

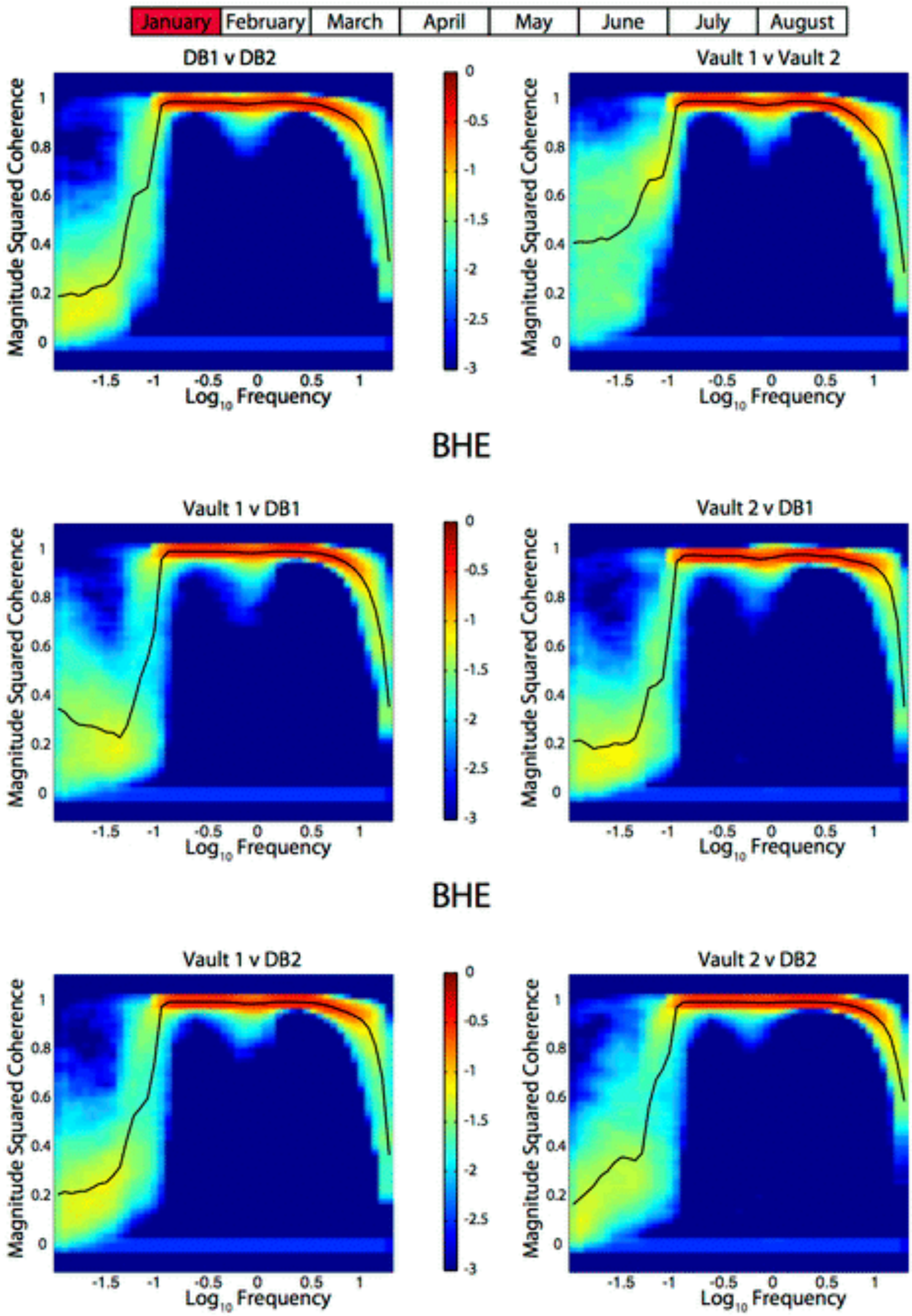
January
February
March
April
May
June
July
August
DB1 v DB2
Vault 1 v Vault 2
BHE
Vault 1 v DB1
Vault 2 v DB1
BHE
Vault 1 v DB2
Vault 2 v DB2
Magnitude Squared Coherence
Log_{10} Frequency

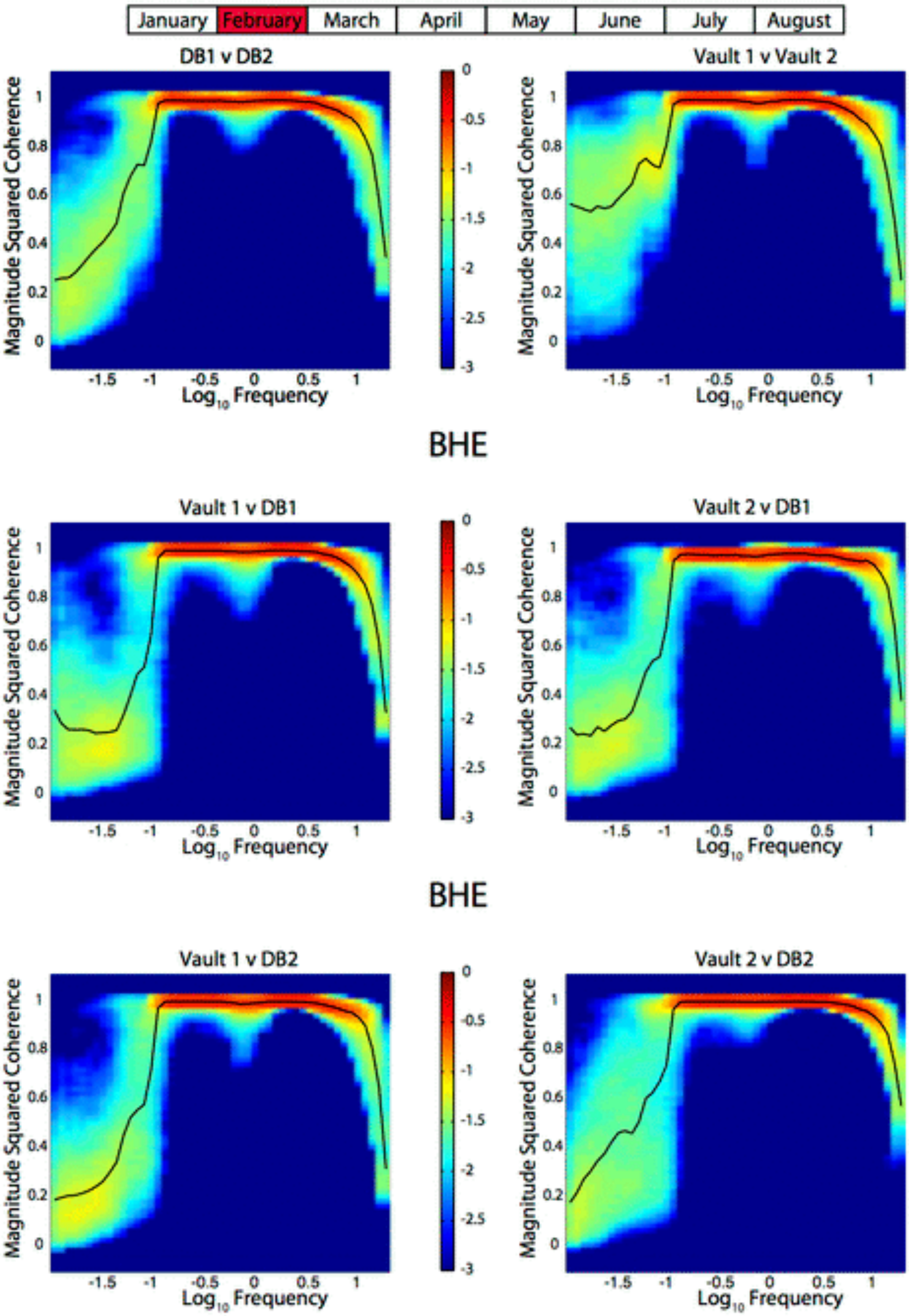
January
February
March
April
May
June
July
August
DB1 v DB2
Vault 1 v Vault 2
BHE
Vault 1 v DB1
Vault 2 v DB1
BHE
Vault 1 v DB2
Vault 2 v DB2
Magnitude Squared Coherence
Log_{10} Frequency

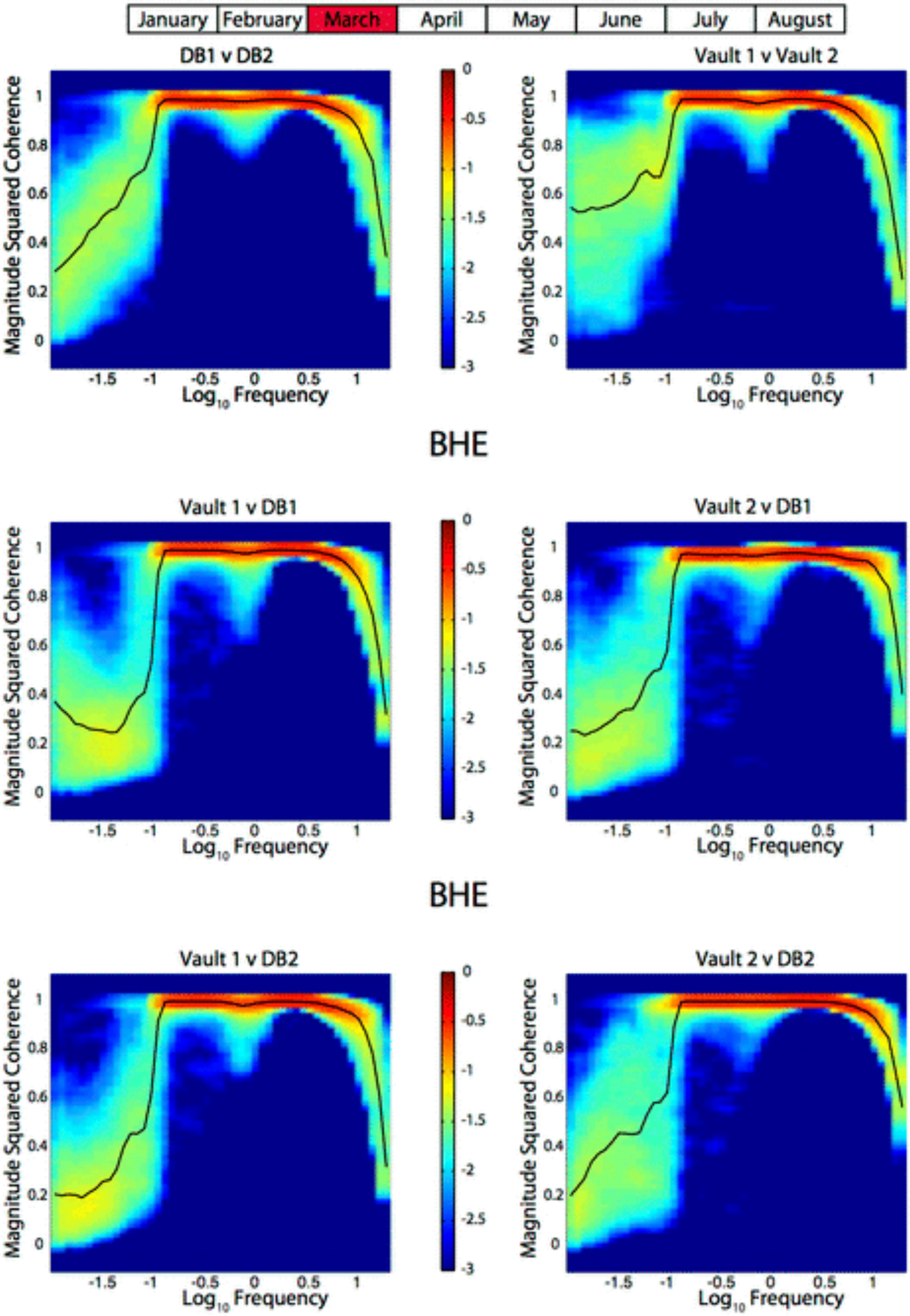
January
February
March
April
May
June
July
August
DB1 v DB2
Vault 1 v Vault 2
BHE
Vault 1 v DB1
Vault 2 v DB1
BHE
Vault 1 v DB2
Vault 2 v DB2
Magnitude Squared Coherence
Log10 Frequency
0
-0.5
-1
-1.5
-2
-2.5
-3

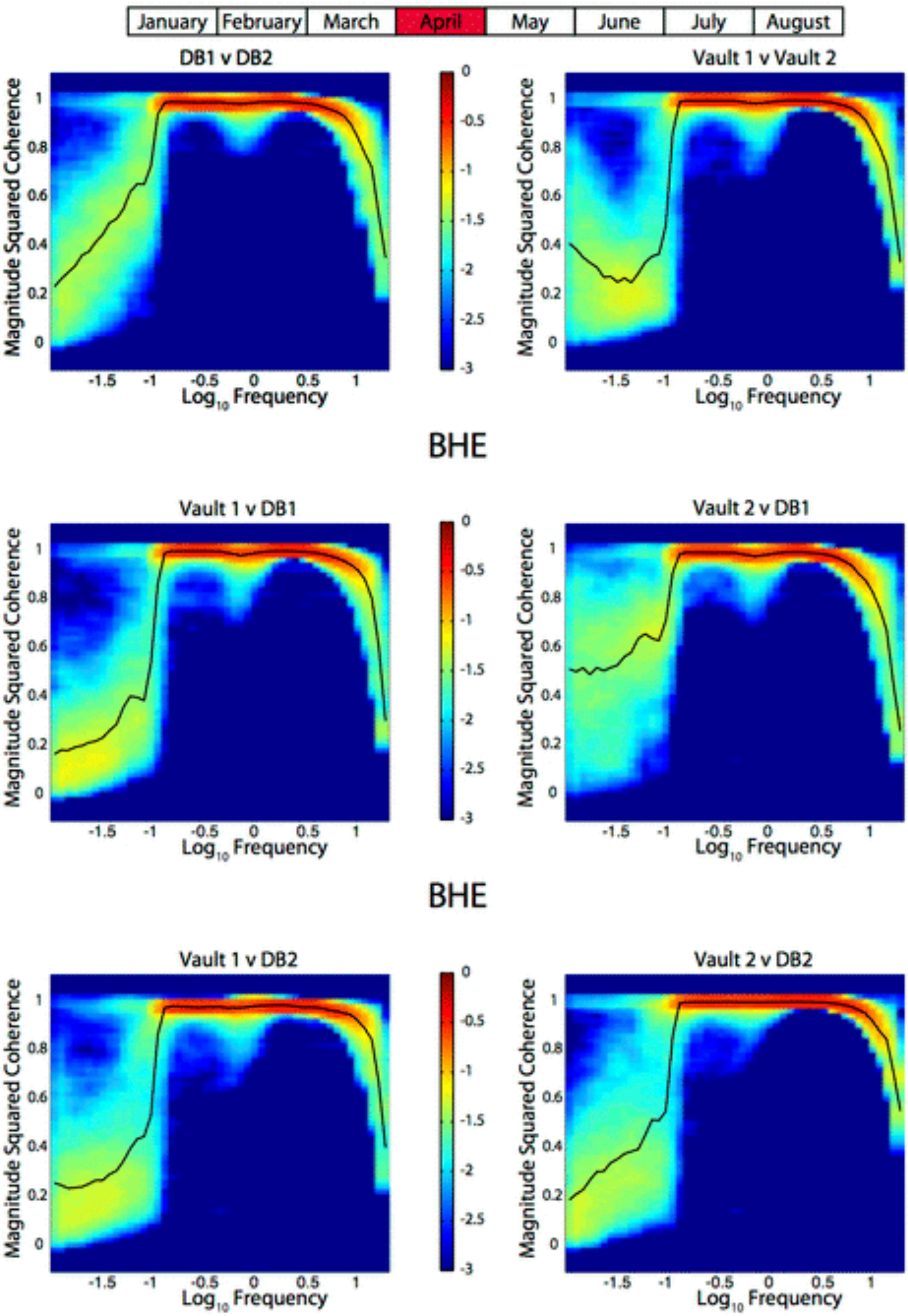
January
February
March
April
May
June
July
August
DB1 v DB2
Vault 1 v Vault 2
BHE
Vault 1 v DB1
Vault 2 v DB1
BHE
Vault 1 v DB2
Vault 2 v DB2
Magnitude Squared Coherence
Log10 Frequency

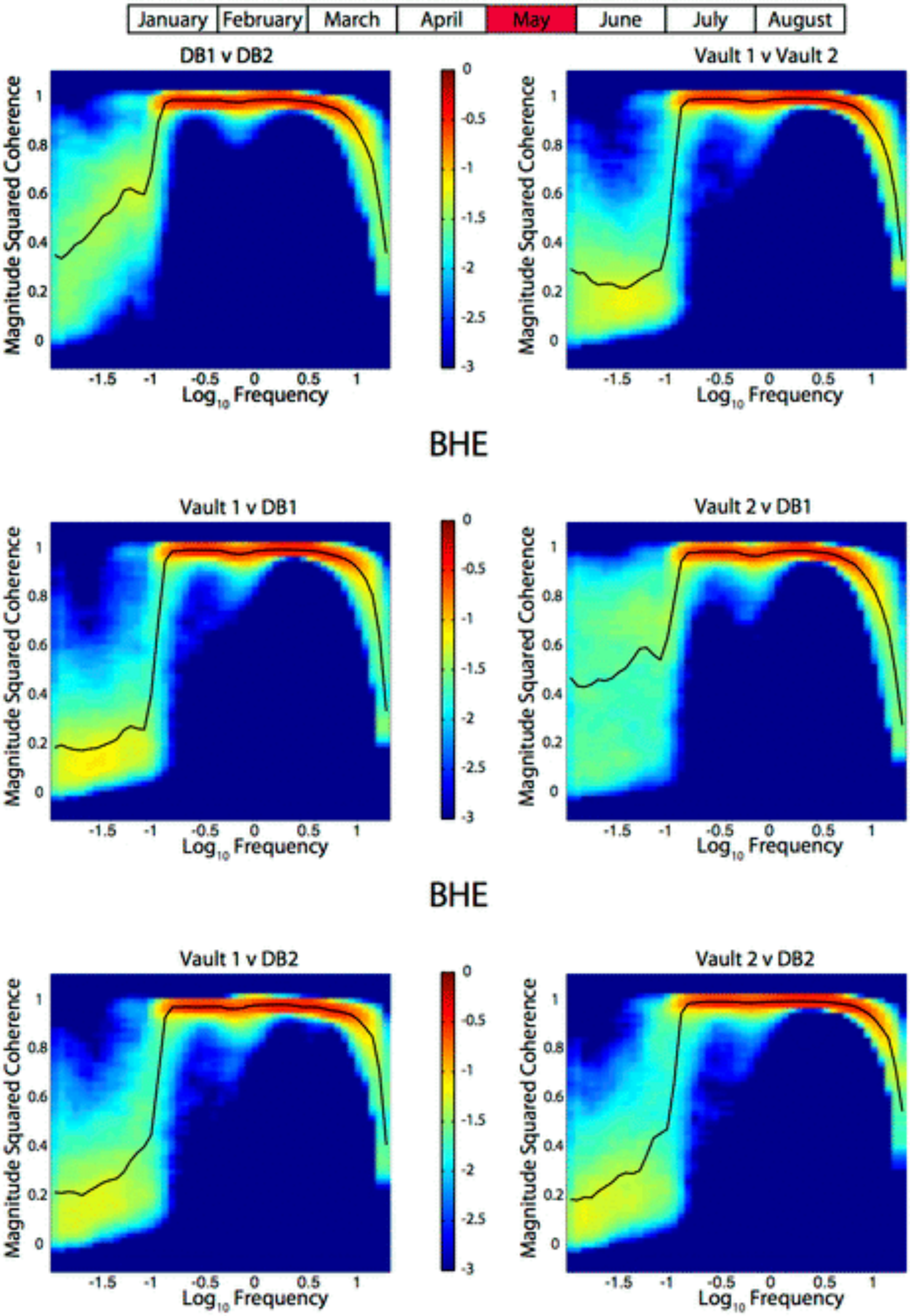

January
February
March
April
May
June
July
August
DB1 v DB2
Vault 1 v Vault 2
BHE
Vault 1 v DB1
Vault 2 v DB1
BHE
Vault 1 v DB2
Vault 2 v DB2
Magnitude Squared Coherence
Log10 Frequency

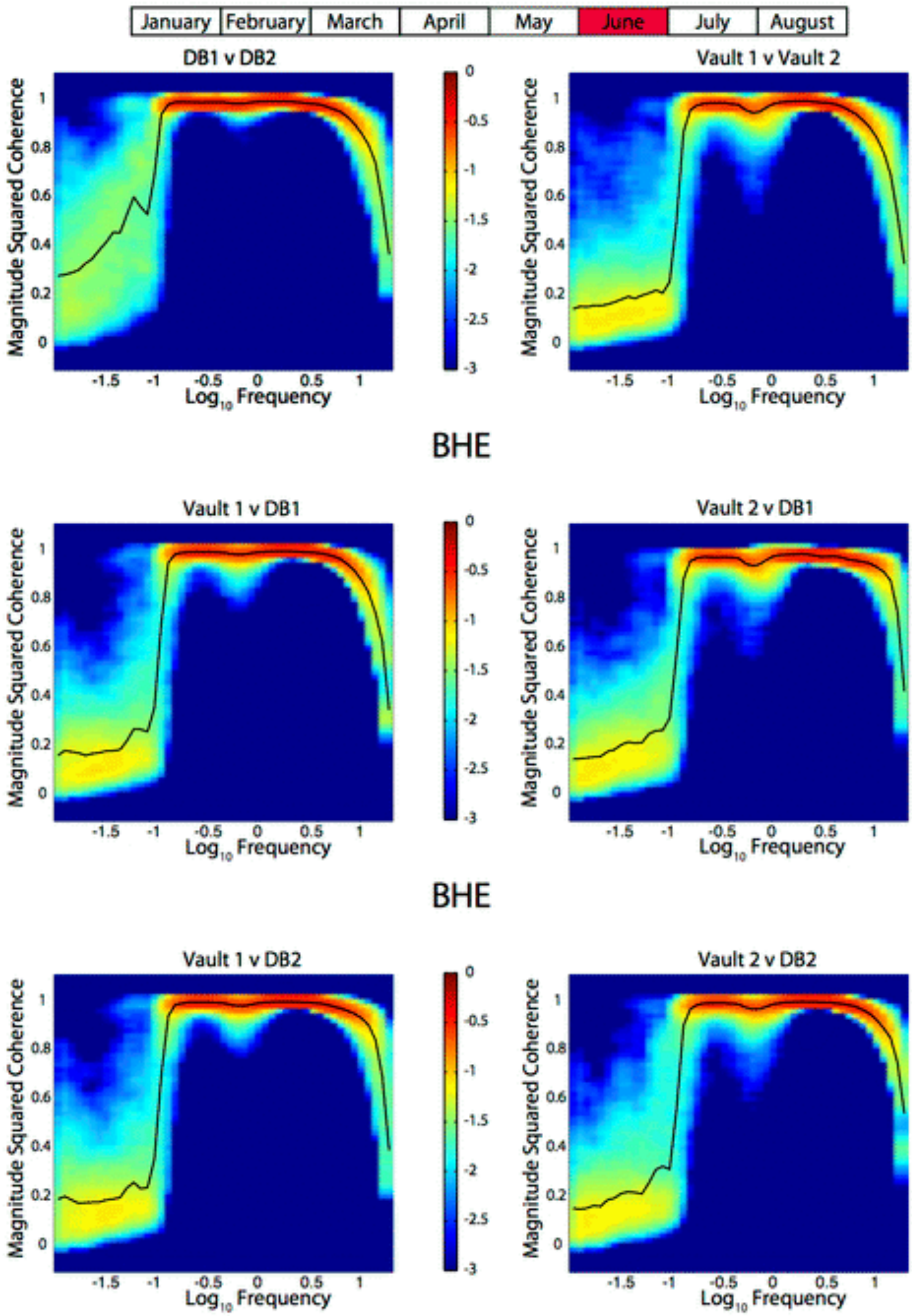
January
February
March
April
May
June
July
August
DB1 v DB2
Vault 1 v Vault 2
BHE
Vault 1 v DB1
Vault 2 v DB1
BHE
Vault 1 v DB2
Vault 2 v DB2
Magnitude Squared Coherence
Log10 Frequency
-1.5 -1 -0.5 0 0.5 1
0 0.2 0.4 0.6 0.8 1
0 -0.5 -1 -1.5 -2 -2.5 -3

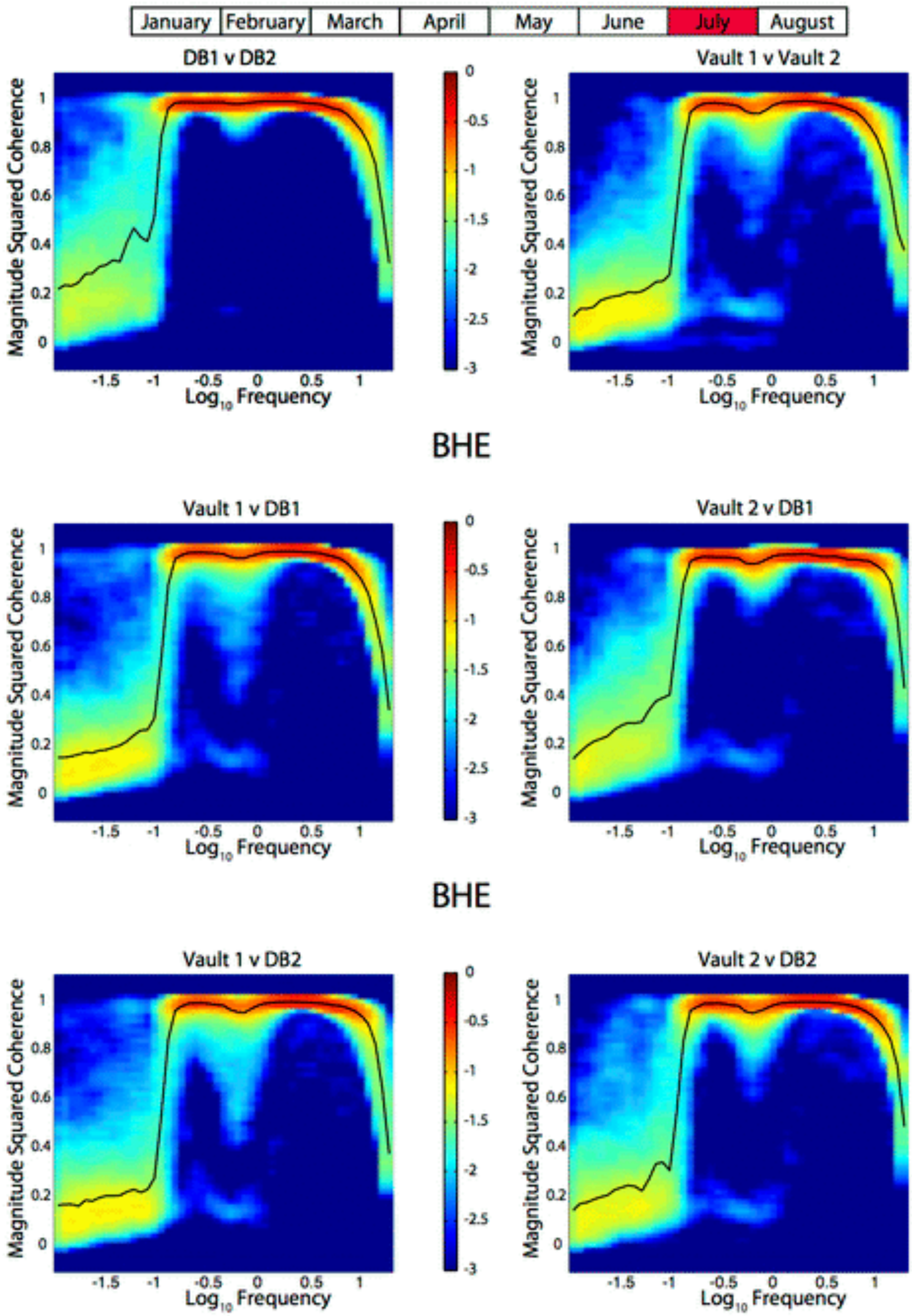
January
February
March
April
May
June
July
August
DB1 v DB2
Vault 1 v Vault 2
BHE
Vault 1 v DB1
Vault 2 v DB1
BHE
Vault 1 v DB2
Vault 2 v DB2
Magnitude Squared Coherence
Log_{10} Frequency

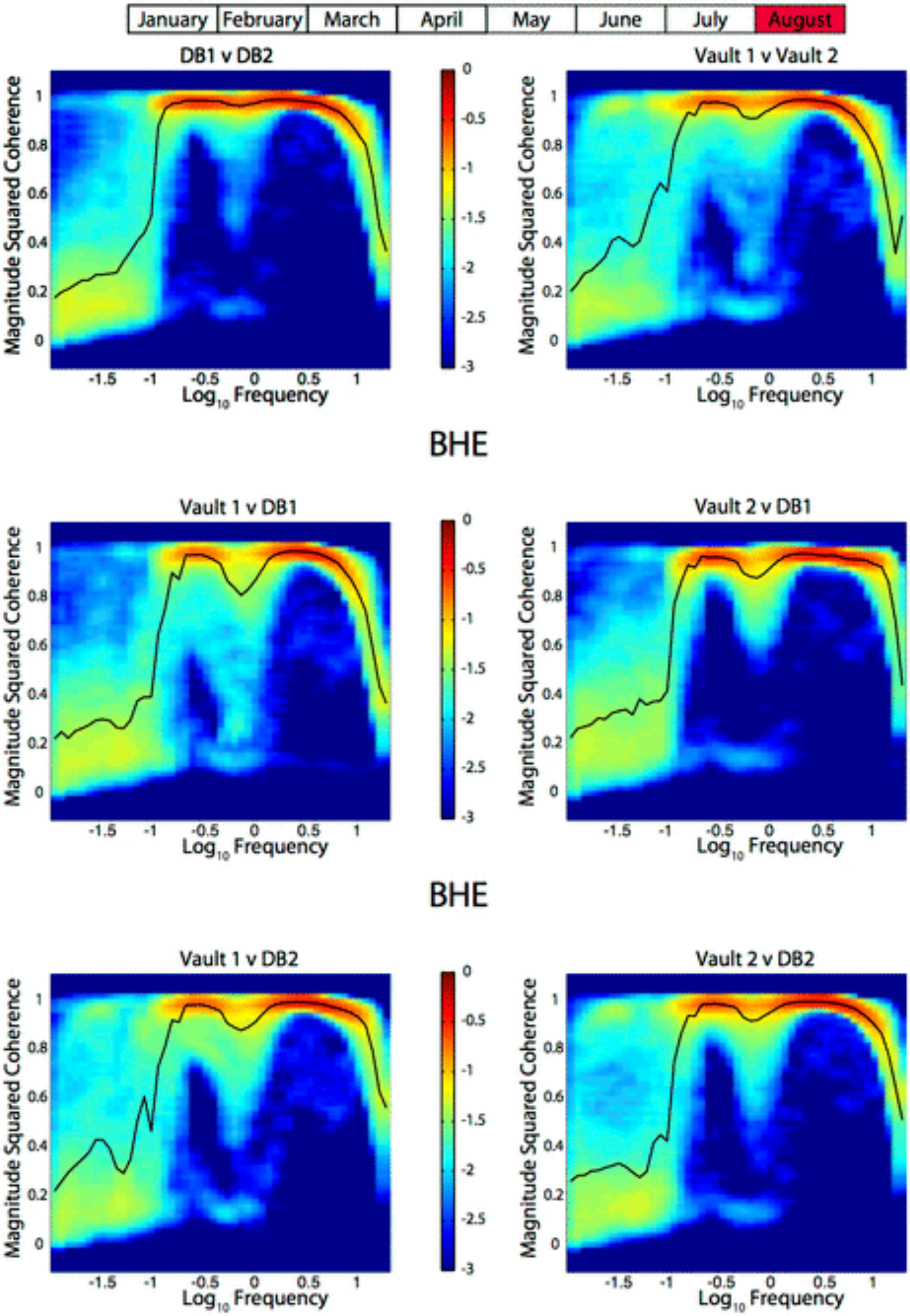
January
February
March
April
May
June
July
August
DB1 v DB2
Vault 1 v Vault 2
BHE
Vault 1 v DB1
Vault 2 v DB1
BHE
Vault 1 v DB2
Vault 2 v DB2
Magnitude Squared Coherence
Log_{10} Frequency
-1.5
-1
-0.5
0
0.5
1
0.2
0.4
0.6
0.8
-2
-2.5
-3

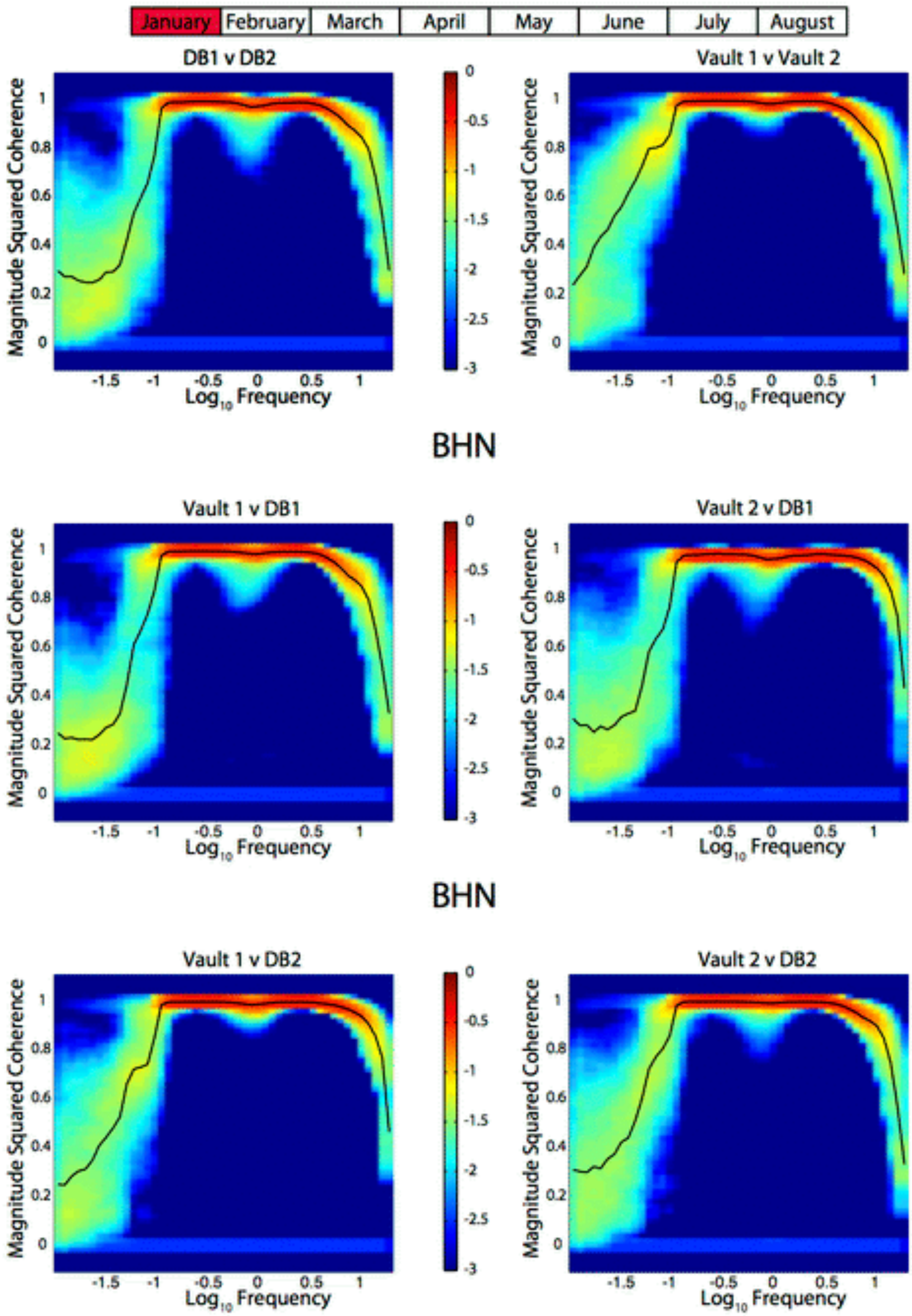
January February March April May June July August
DB1 v DB2
Vault 1 v Vault 2
BHN
Vault 1 v DB1
Vault 2 v DB1
BHN
Vault 1 v DB2
Vault 2 v DB2
Magnitude Squared Coherence
Log_{10} Frequency

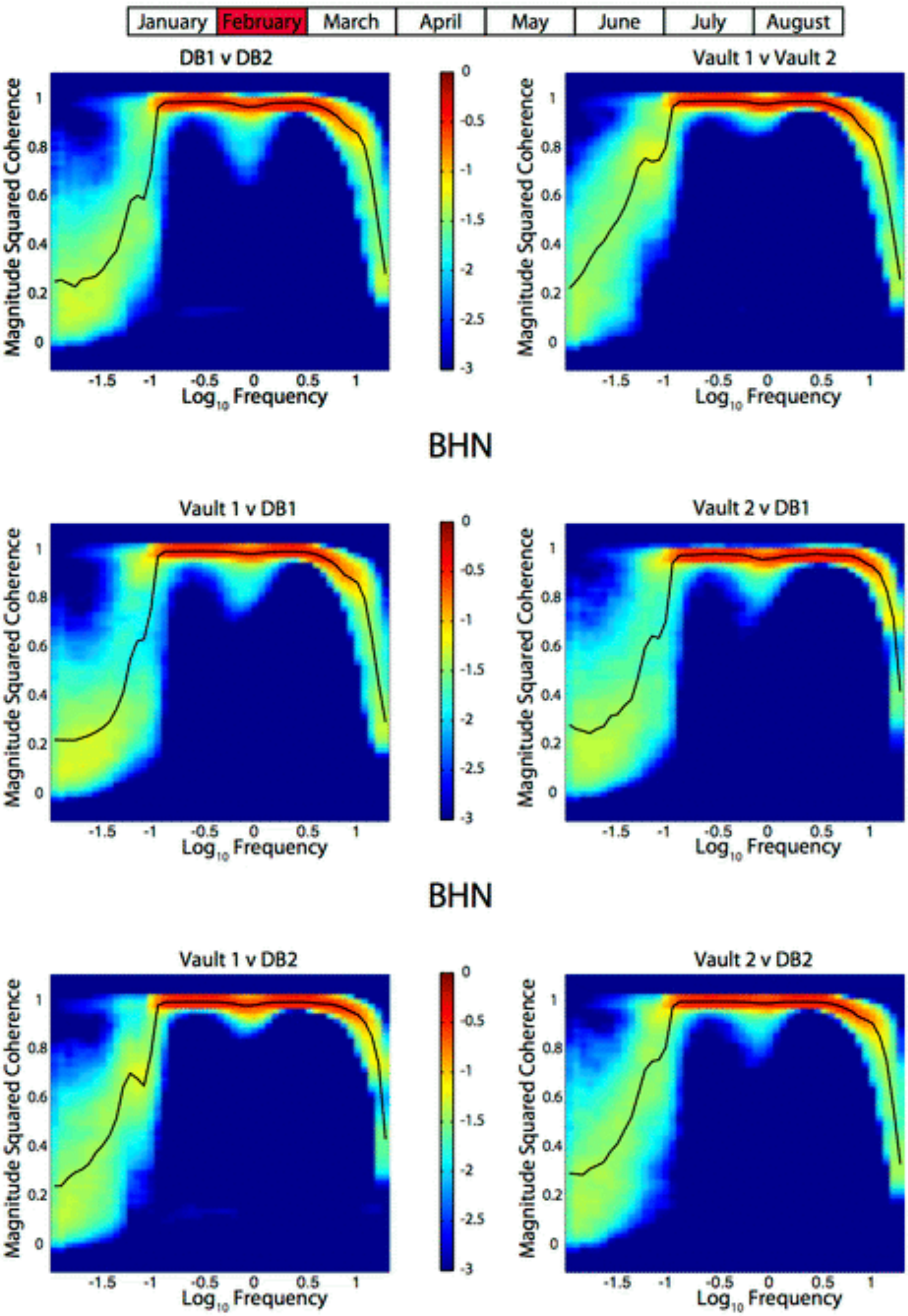
January
February
March
April
May
June
July
August
DB1 v DB2
Vault 1 v Vault 2
BHN
Vault 1 v DB1
Vault 2 v DB1
BHN
Vault 1 v DB2
Vault 2 v DB2
Magnitude Squared Coherence
Log$_{10}$ Frequency
-1.5
-1
-0.5
0
0.5
1
0.8
0.6
0.4
0.2
-2
-2.5
-3

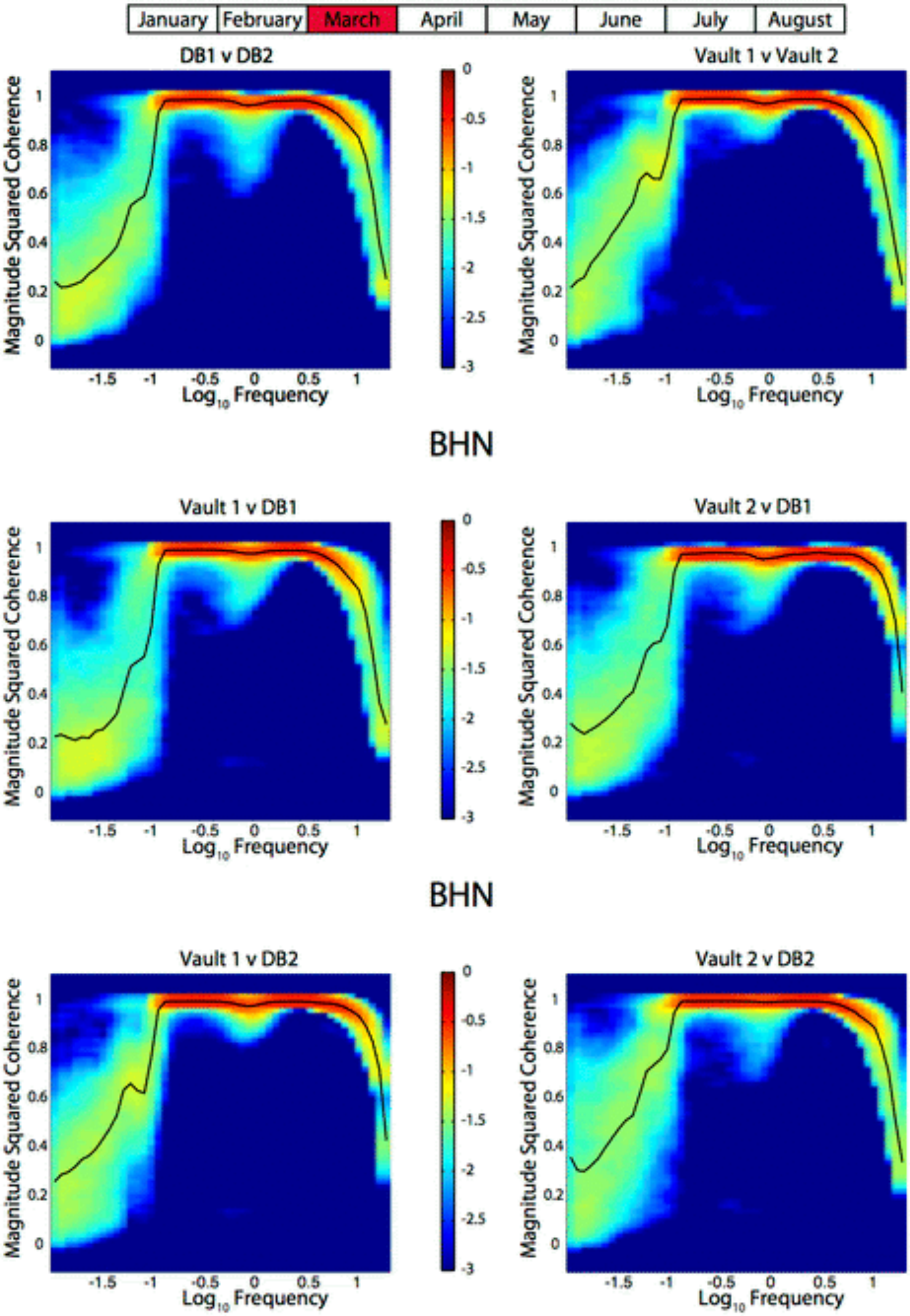
January
February
March
April
May
June
July
August
DB1 v DB2
Vault 1 v Vault 2
BHN
Vault 1 v DB1
Vault 2 v DB1
BHN
Vault 1 v DB2
Vault 2 v DB2
Magnitude Squared Coherence
Log_{10} Frequency
0
-0.5
-1
-1.5
-2
-2.5
-3

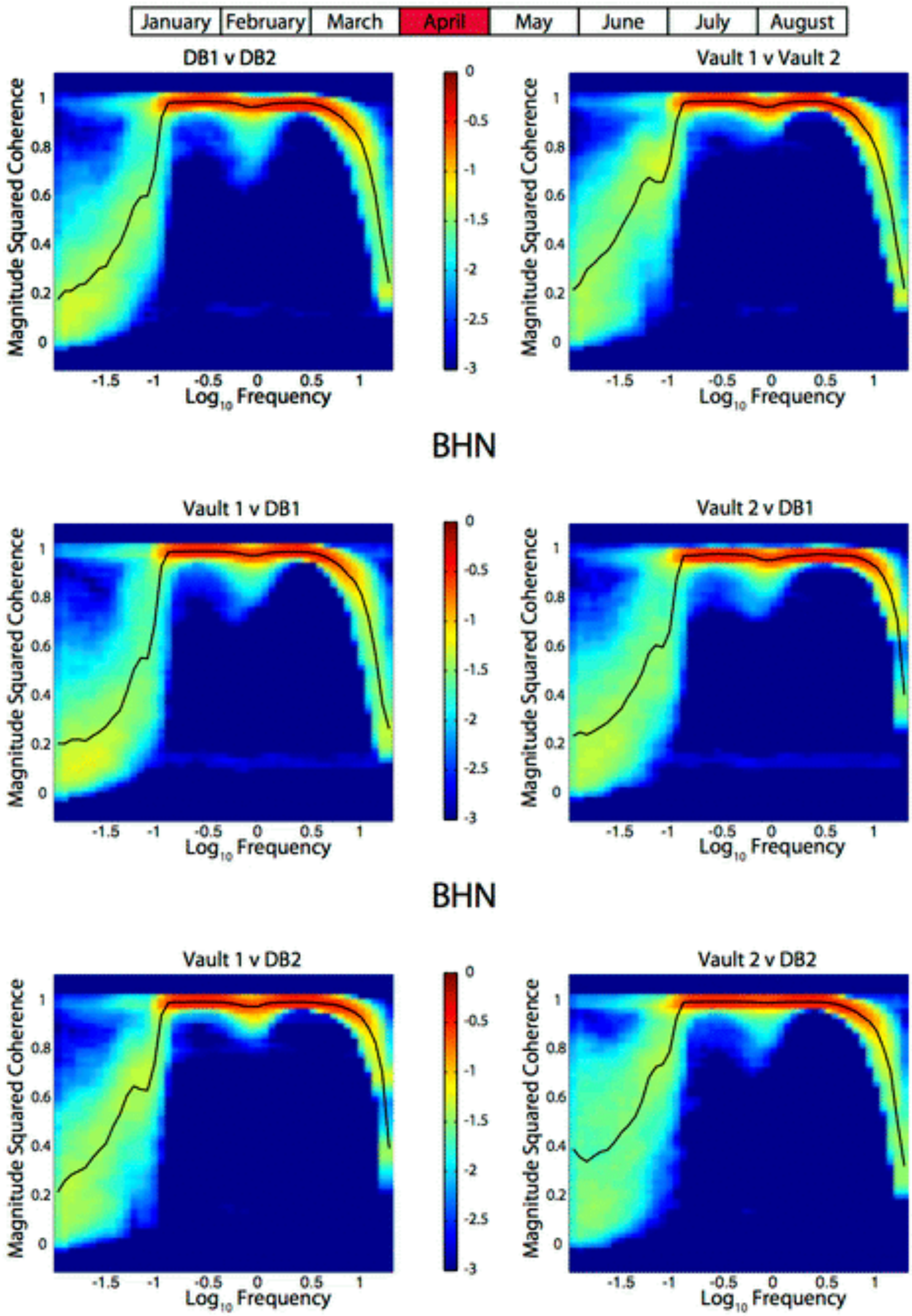
January
February
March
April
May
June
July
August
DB1 v DB2
Vault 1 v Vault 2
BHN
Vault 1 v DB1
Vault 2 v DB1
BHN
Vault 1 v DB2
Vault 2 v DB2
Magnitude Squared Coherence
$\mathrm{Log_{10}}$ Frequency
0
-0.5
-1
-1.5
-2
-2.5
-3

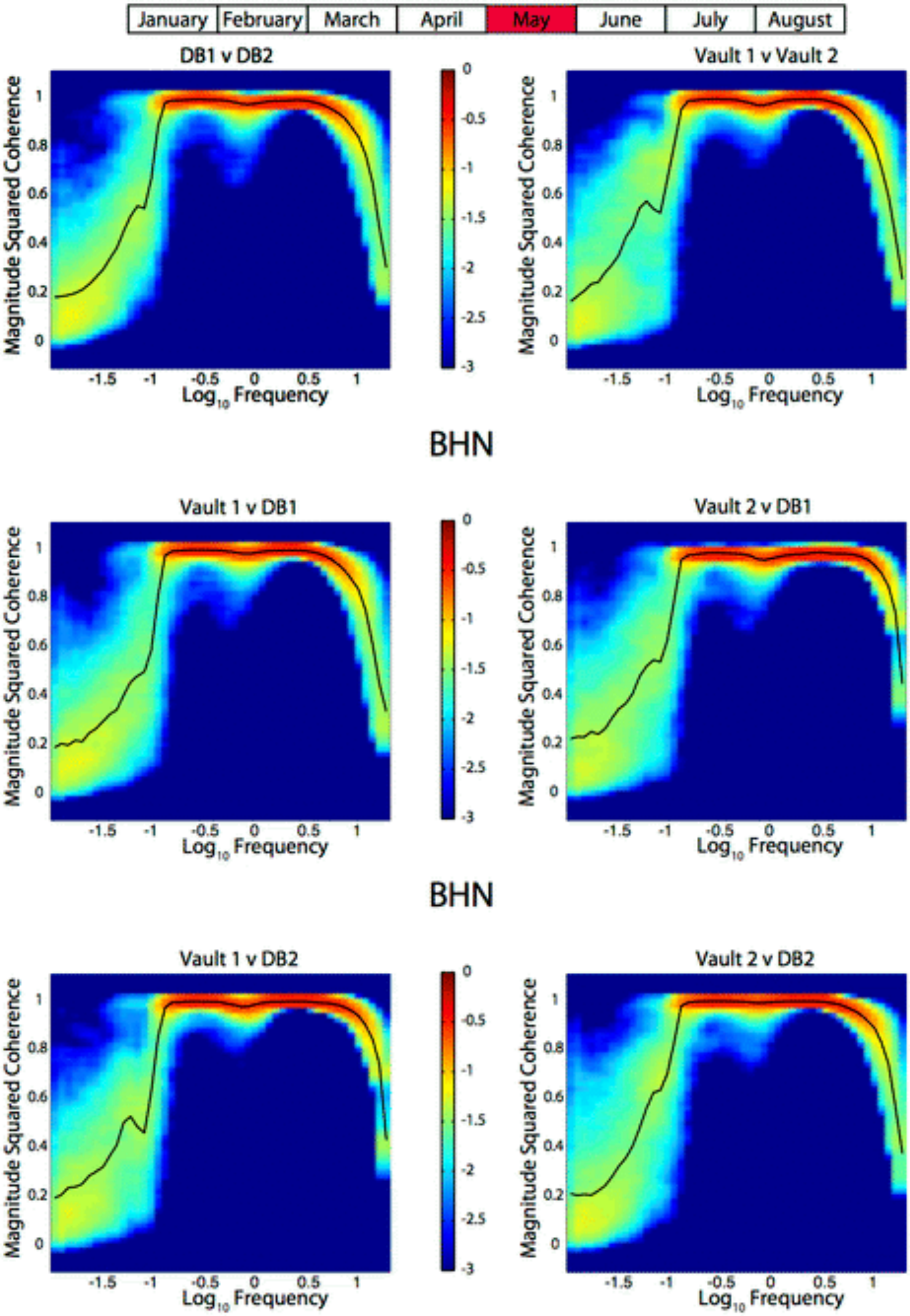
January
February
March
April
May
June
July
August
DB1 v DB2
Vault 1 v Vault 2
BHN
Vault 1 v DB1
Vault 2 v DB1
BHN
Vault 1 v DB2
Vault 2 v DB2
Magnitude Squared Coherence
Log10 Frequency

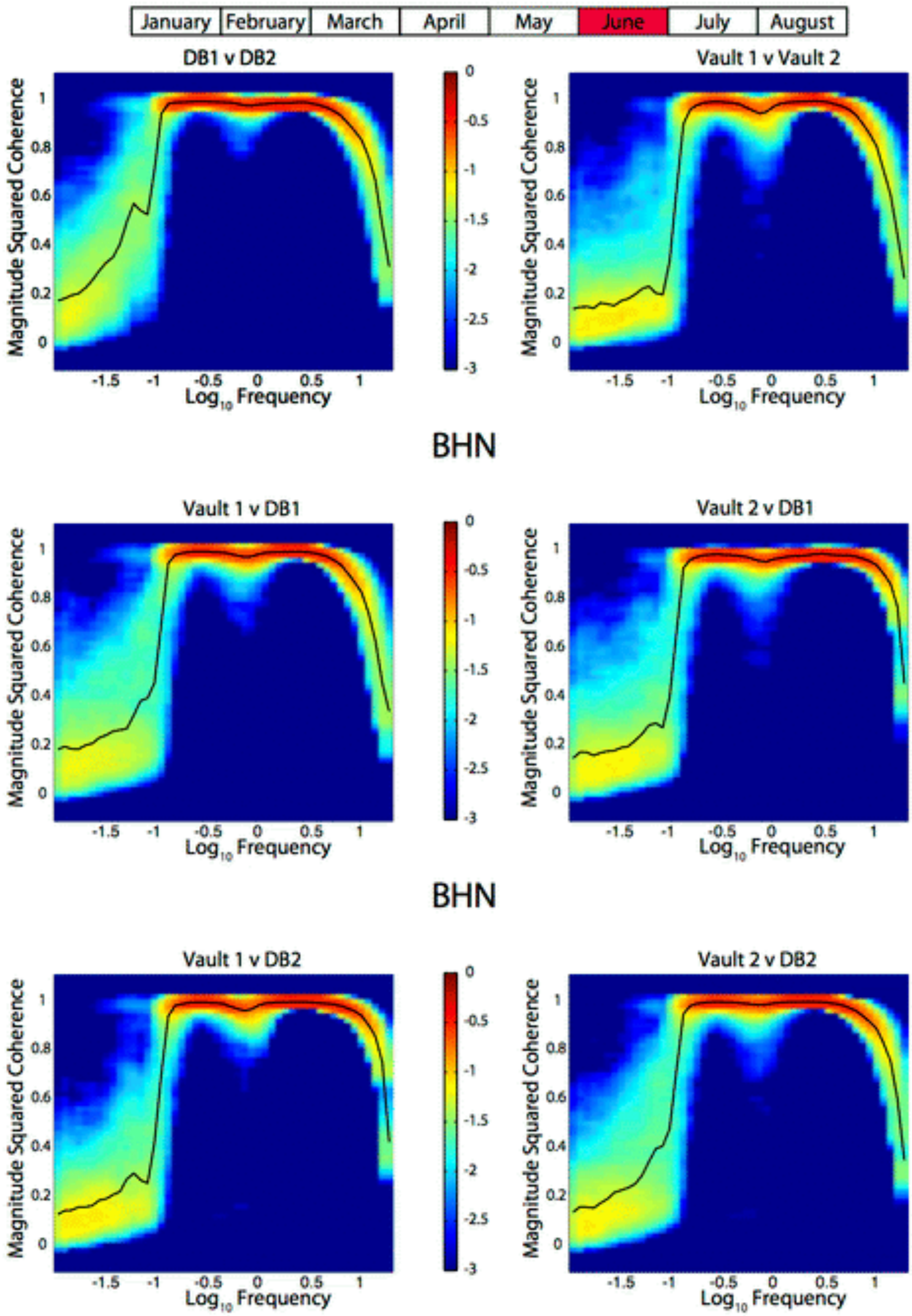
January
February
March
April
May
June
July
August
DB1 v DB2
Vault 1 v Vault 2
BHN
Vault 1 v DB1
Vault 2 v DB1
BHN
Vault 1 v DB2
Vault 2 v DB2
Magnitude Squared Coherence
Log_{10} Frequency

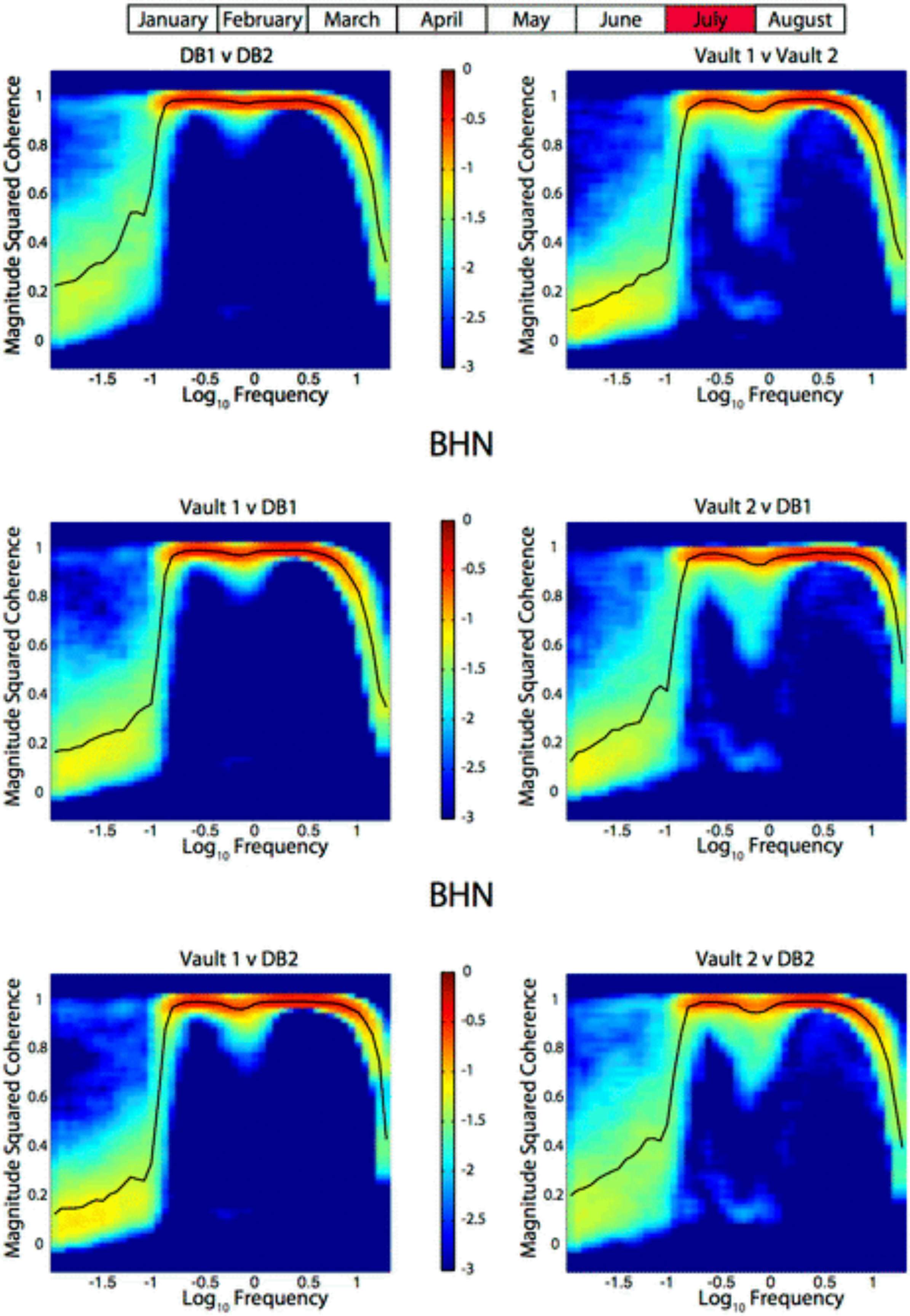

January
February
March
April
May
June
July
August
DB1 v DB2
Vault 1 v Vault 2
BHN
Vault 1 v DB1
Vault 2 v DB1
BHN
Vault 1 v DB2
Vault 2 v DB2
Magnitude Squared Coherence
Log10 Frequency

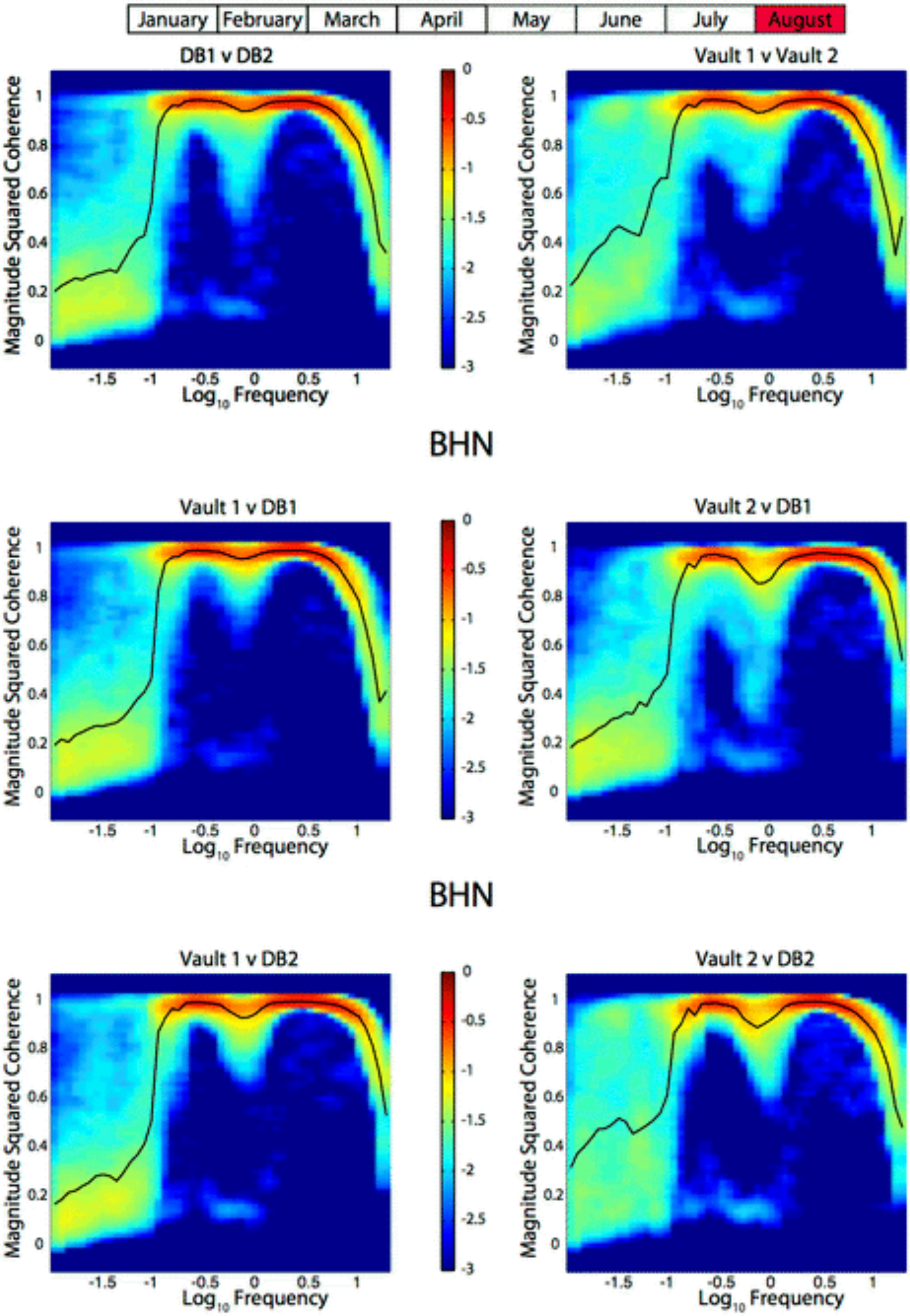
January
February
March
April
May
June
July
August
DB1 v DB2
Vault 1 v Vault 2
BHN
Vault 1 v DB1
Vault 2 v DB1
BHN
Vault 1 v DB2
Vault 2 v DB2
Magnitude Squared Coherence
Log10 Frequency